

1

General Properties of Nitrides

Introduction

GaN as a representative of its binary cousins, InN and AlN, and their ternaries along with the quaternary, is considered one of the most important semiconductors after Si. It is no wonder that it finds ample applications in lighting and displays of all kinds, lasers, detectors, and high-power amplifiers. These applications stem from the excellent optical and electrical properties of nitride semiconductors. The parameters are imperative in determining the utility and applicability of this class of materials to devices, as will be made evident in this chapter and throughout the book.

In this chapter, the structural, mechanical, thermal, chemical, electrical, and optical properties of GaN and its binary cousins as well as the substrates commonly used for nitride epitaxy are treated in a general sense for quick reference. The detailed properties associated with electrical and optical parameters and properties are discussed in chapters dealing with transport and optical processes in GaN and related alloys. Because GaN is used in the form of a thin film deposited on foreign substrates, meaning templates other than GaN, a discussion of heteroepitaxial thin films is of paramount importance. Consequently, the properties of nitride films intricately depend on substrates, inclusive of the inherent properties such as lattice constants and thermal expansion coefficients, and on the process-induced characteristics such as surface preparation and chemical and physical interactions at the surface. These too are discussed in the book.

1.1

Crystal Structure of Nitrides

Group III nitrides can be of crystalline structures: the *wurtzite* (Wz), *zinc blende* (ZB), and *rock salt*. Under ambient conditions, the thermodynamically stable structure is wurtzite for bulk AlN, GaN, and InN. The zinc blende structure for GaN and InN has been stabilized by epitaxial growth of thin films on {0 1 1} crystal planes of cubic substrates such as Si [1], SiC [2], MgO [3], and GaAs [4]. In these cases, the intrinsic tendency to form the Wz structure is overcome by the topological compatibility.

However, Wz structure could very likely be present at the extended defect sites. The rock salt form is possible only under high pressures and, therefore, is laboratory form of exercise.

Let us now discuss the space groups for the various forms of nitrides. The rock salt, or NaCl, structure (with space group $Fm\bar{3}m$ in the Hermann–Mauguin notation and O_h^5 in the Schoenflies notation) can be induced in AlN, GaN, and InN under very high pressures. The reason for this is that the reduction of the lattice dimensions causes the interionic Coulomb interaction to favor the ionicity over the covalent nature. The structural phase transition to rock salt structure was experimentally observed at the following estimated pressure values: 22.9 GPa (17 GPa in other estimates) for AlN [5], 52.2 GPa for GaN [6], and 12.1 GPa for InN [7]. Rock salt III nitrides cannot be produced by any epitaxial growth.

The space grouping for the zinc blende structure is $F\bar{4}3m$ in the Hermann–Mauguin notation and T_d^2 in the Schoenflies notation. The zinc blende structure has a cubic unit cell, containing four group III elements and four nitrogen elements. (Although the term zinc blende originated in compounds such as ZnS, which could be in cubic or hexagonal phase, it has been used ubiquitously for compound semiconductors with cubic symmetry. The correct term that should be used for the cubic phase of GaN is actually sphalerite. However, to be consistent with the usage throughout the literature, even at the expense of accuracy, the term zinc blende has been used in this book). The position of the atoms within the unit cell is identical to the diamond crystal structure. Both structures consist of two interpenetrating face-centered cubic sublattices, offset by one quarter of the distance along a body diagonal. Each atom in the structure may be viewed as positioned at the center of a tetrahedron, with its four nearest neighbors defining the four corners of the tetrahedron. The stacking sequence for the (1 1 1) close-packed planes in this structure is AaBbCc. Lowercase and uppercase letters stand for the two different kinds of constituents.

The wurtzite structure has a hexagonal unit cell and thus two lattice constants, c and a . It contains six atoms of each type. The space grouping for the wurtzite structure is $P6_3mc$ in the Hermann–Mauguin notation and C_{6v}^4 in the Schoenflies notation. The point group symmetry is 6 mm in the Hermann–Mauguin notation and C_{6v} in the Schoenflies notation. The Wz structure consists of two interpenetrating *hexagonal close-packed* (hcp) sublattices, each with one type of atom, offset along the c -axis by $5/8$ of the cell height ($5c/8$). The wurtzite and zinc blende structures are somewhat similar and yet different. In both cases, each group III atom is coordinated by four nitrogen atoms. Conversely, each nitrogen atom is coordinated by four group III atoms. The main difference between these two structures lies in the stacking sequence of closest packed diatomic planes. The Wz structure consists of alternating biatomic close-packed (0 0 0 1) planes of Ga and N pairs, thus the *stacking sequence* of the (0 0 0 1) plane is AaBbAa in the (0 0 0 1) direction.

Although the main interest is in Wz GaN as opposed to zinc blende GaN, a description of stacking sequence of both GaN polytypes with the accepted Ramsdel notation is warranted, so is the stacking order of SiC polytypes that are relevant to GaN because they are used for substrates in GaN epitaxy. Therefore, a generic description of stacking in Wz semiconductors is given below. A comprehensive description of the tetrahedrally coordinated structures is imperative for a clear picture

of nitride semiconductors, particularly the extended defects that are discussed in detail in Chapter 4. The bonds describe a tetrahedron denoted by T, which has one atom species at each of the three corners and the other atom species in its center [8,9]. The basal plane of this structure is defined by one face of the tetrahedron and the bond perpendicular to this plane defines the c -axis. A rotation of 180° around the c -axis produces a twin variant denoted by T' as shown in Figure 1.1a (left).

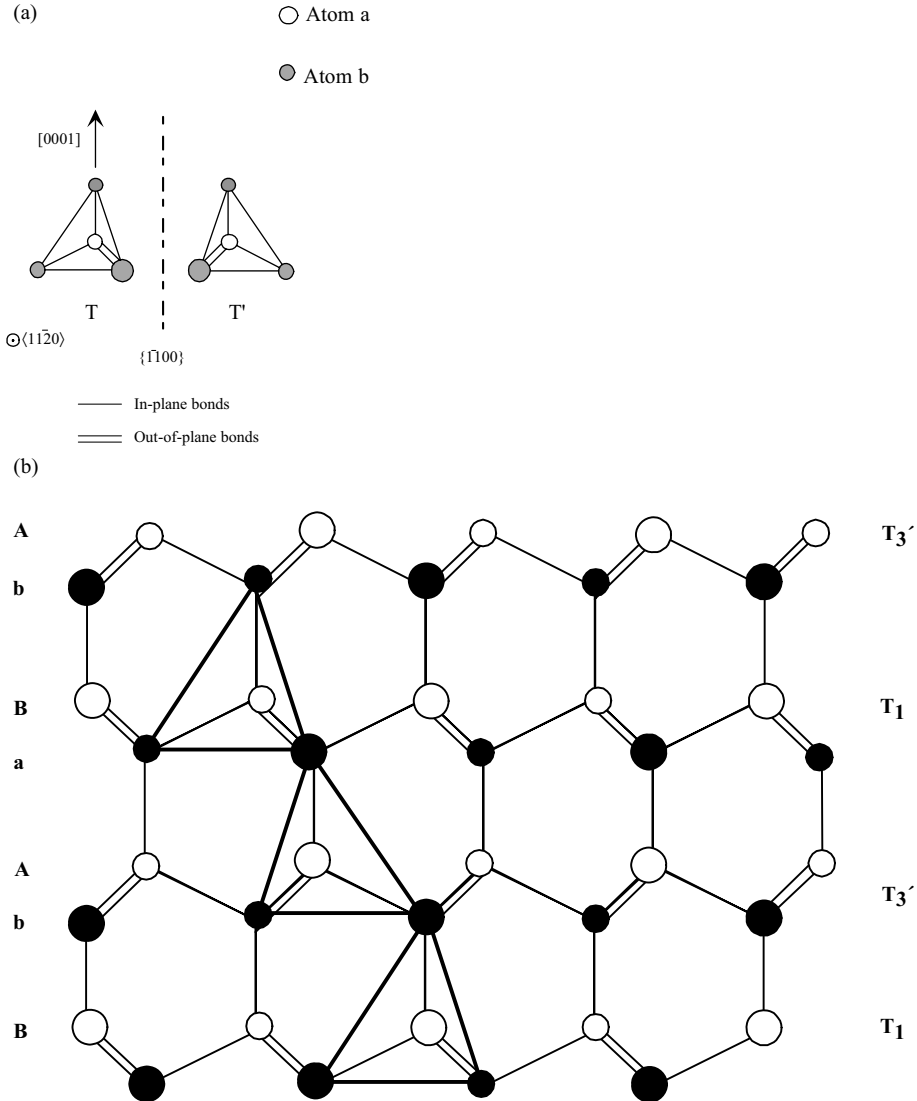


Figure 1.1 Representation of the tetrahedrally coordinated materials in the Ramsdel notation. (a) The two possible tetrahedra. (b) The T₁, T₃, T₁, T₃, tetrahedral stacking composing the 2H sequence. Courtesy of Pierre Ruterana [9].

The two variants (twins T and T') are related to one another by mirror symmetry about one of the $\{1\bar{1}00\}$ *m*-planes. A tetrahedron can occupy one of the three possible positions in the basal plane. The representation of the tetrahedrally coordinated materials in the Ramsdel notation is shown in Figure 1.1a for two possible tetrahedra, one is the mirror image twin of the other with respect to the $(1\bar{1}00)$ *m*-plane. The single bonds are on the $(11\bar{2}0)$ plane, called the *a*-plane. The layers of the tetrahedra can then be denoted by T₁, T₂, T₃, and by T'₁, T'₂, T'₃ for its twin. An example of T₁, T'₁, T₁, T'₃ stacking order representing 2H ordering as in wurtzitic GaN is shown in Figure 1.1b. The structure of nitride semiconductors and most relevant polytypes of SiC can be completely described by a combinatorial stacking of the aforementioned six tetrahedra layers. Naturally, not all the stacking sequences must obey the following two rules to keep a corner sharing structure, as such not all stacking orders are allowed:

- (i) A tetrahedron T can be followed by another one of the same kind with the following subscript: T₁T₂T₃, and inversely for the twin variant: T'₃T'₂T'₁.
- (ii) A tetrahedron T₁ must be followed by the twin variant of the preceding subscript: T₁T'₃, and inversely for its twin variant: T'₁T₂.

In the Ramsdel notation, the stacking order for the wurtzite structure corresponding to various polytypes can be denoted as

- T₁T'₃ or T₂T'₁ or T₃T'₂ for the 2H polytype, which is also applicable to Wz nitride semiconductors;
- T₁T₂T'₁T'₃ for the 4H polytype;
- T₁T₂T₃T'₂T'₁T'₃ for the 6H polytype;
- T₁T₂T₃ or T'₃T'₂T'₁ for the 3C polytype.

The 3C, 4H, and 6H stacking sequences as well as 2H sequence on 6H sequence are discussed in Chapter 3.

Recall that GaN crystallizes in the cubic structure (zinc blende or sphalerite, the latter being the correct term and the former being the one used universally) or in the more stable hexagonal structure (wurtzite). The anions (N³⁻) form an hcp structure in which the cations (Ga³⁺) occupy half of the tetrahedral sites. The structure of a unit cell of GaN projected along $[0001]$ is depicted schematically in Figure 1.2. The open symbols represent γ sites that are occupied by nitrogen atoms; the Ga atoms are in the tetrahedral sites, β . These latter sites can either be at heights $(3/8)c$ above (β_1) or below (β_2) N site, depending on the crystal polarity.

A stick-and-ball representation of Ga-polarity and N-polarity Wz structure is depicted in Figure 1.3. The Wz and zinc blende structures differ only in the bond angle of the second nearest neighbor (Figure 1.4). As clearly shown, the stacking order of the Wz along the $[0001]$ *c*-direction is AaBb, meaning a mirror image but no in-plane rotation with the bond angles. In the zinc blende structure along the $[111]$ direction, there is a 60° rotation that causes a stacking order of AaBbCc. The point with regard to rotation is illustrated in Figure 1.4b. The nomenclature for various commonly used planes of hexagonal semiconductors in two- and three-dimensional versions is presented in Figures 1.5 and 1.6. The Wz group III nitrides lack an

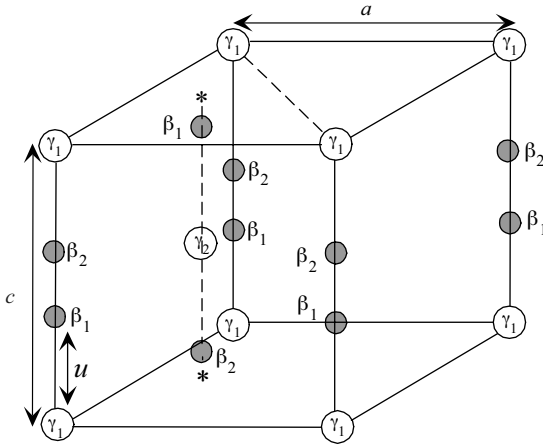


Figure 1.2 Schematic diagram showing the β_1 and β_2 tetrahedral sites of GaN unit cell. Starting with the assumption that N occupies the γ sites, only one family of β sites can be simultaneously occupied by Ga atoms. Courtesy of Pierre Ruterana [9].

inversion plane perpendicular to the c -axis; thus, nitride surfaces have either a group III element (Al, Ga, or In) polarity (referred to as Ga-polarity) with a designation of (0001) or $(0001)A$ plane or a N-polarity with a designation of $(000\bar{1})$ or $(0001)B$ plane. We will use the former notations for each. The distinction between these two directions is essential in nitrides because of their implications for the polarity of the polarization charge. Three surfaces and directions are of special importance in

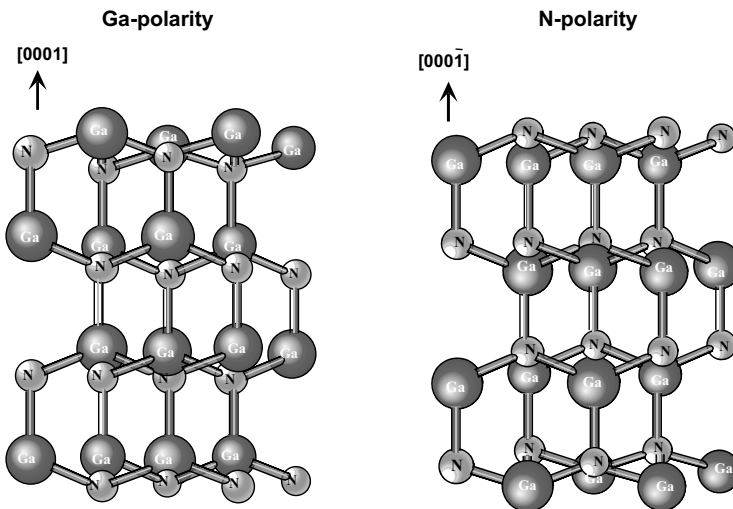


Figure 1.3 A stick-and-ball diagram of a hexagonal structure.

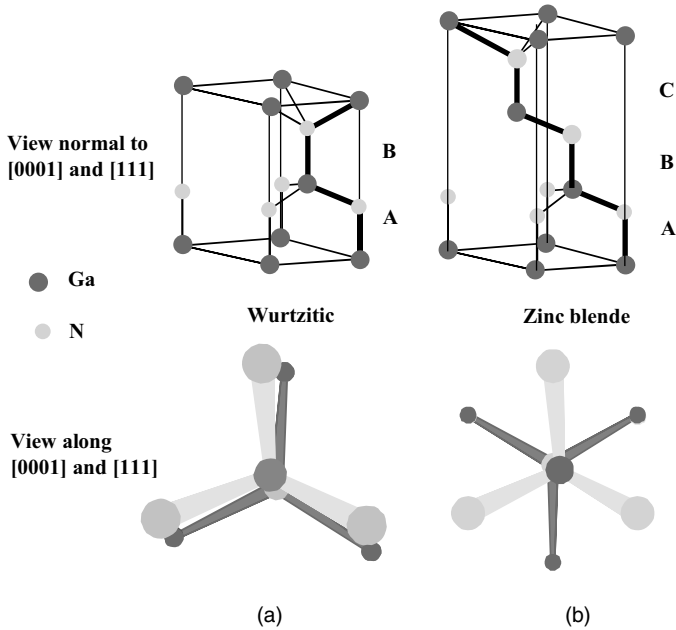


Figure 1.4 A stick-and-ball stacking model of crystals with (a, both top and bottom) 2H wurtzitic and (b, both top and bottom) 3C zinc blende polytypes. The bonds in an A-plane ($1\bar{1}\bar{2}0$) are indicated with heavier lines to accentuate the stacking sequence. The figures on top depict the three-dimensional view. The

figures at the bottom indicate the projections on the (0001) and (111) planes for wurtzitic and cubic phases, respectively. Note the rotation in the zinc blende case along the $\langle 111 \rangle$ direction. (Please find a color version of this figure on the color tables.)

nitrides, which are (0001) c -, $(1\bar{1}\bar{2}0)$ a -, and $(1\bar{1}00)$ m -planes and the directions associated with them, $\langle 0001 \rangle$, $\langle 11\bar{2}0 \rangle$, and $\langle 1\bar{1}00 \rangle$ as shown in Figure 1.7. The (0001) , or the basal plane, is the most commonly used surface for growth. The other two are important in that they represent the primary directions employed in reflection high-energy electron diffraction (RHEED) observations in molecular beam epitaxial growth, apart from being perpendicular to one another. They also represent the direction of stripes employed in the *epitaxial lateral overgrowth* (ELO), details of which are discussed in Section 3.5.5.2.

The cohesive energy per bond in the wurtzite form is 2.88 eV ($63.5 \text{ kcal mol}^{-1}$), 2.2 eV ($48.5 \text{ kcal mol}^{-1}$), and 1.93 eV ($42.5 \text{ kcal mol}^{-1}$) for AlN, GaN, and InN, respectively [10]. The calculated energy difference $\Delta E_{\text{W-ZB}}$ between wurtzite and zinc blende lattice is small [11]: $\Delta E_{\text{W-ZB}} = -18.41 \text{ meV/atom}$ for AlN, $\Delta E_{\text{W-ZB}} = -11.44 \text{ meV/atom}$ for InN, and $\Delta E_{\text{W-ZB}} = -9.88 \text{ meV/atom}$ for GaN. Wurtzite form is energetically preferable for all three nitrides compared to zinc blende, although the energy difference is small.

The Wz structure can be represented by lattice parameters a in the basal plane and c in the perpendicular direction, and the *internal parameter* u , as shown in Figure 1.8.

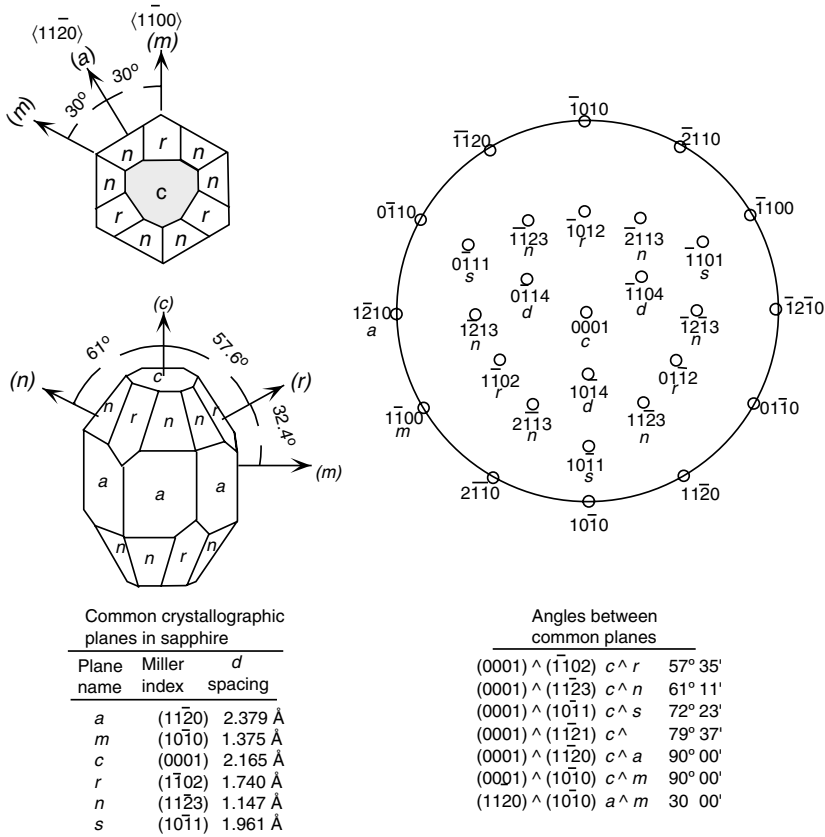


Figure 1.5 Labeling of planes in hexagonal symmetry (* for sapphire).

The u parameter is defined as the anion–cation bond length (also the nearest neighbor distance) divided by the c lattice parameter. The c parameter depicts the unit cell height. The wurtzite structure is a hexagonal close-packed lattice, comprising vertically oriented X–N units at the lattice sites. The *basal plane lattice parameter* (the edge length of the basal plane hexagon) is universally depicted by a and the *axial lattice parameter*, perpendicular to the basal plane, is universally described by c . The interatomic distance in the basic unit is described by the internal parameter u . In an ideal wurtzite structure represented by four touching hard spheres, the values of the axial ratio and the internal parameter are $c/a = \sqrt{8/3} = 1.633$ and $u = 3/8 = 0.375$, respectively. The crystallographic vectors of wurtzite are $\vec{a} = a(1/2, \sqrt{3}/2, 0)$, $\vec{b} = a(1/2, -\sqrt{3}/2, 0)$, and $\vec{c} = a(0, 0, c/a)$. In Cartesian coordinates, the basis atoms are $(0, 0, 0)$, $(0, 0, uc)$, $a(1/2, \sqrt{3}/6, c/2a)$, and $a(1/2, \sqrt{3}/6, [u + 1/2]c/a)$.

Table 1.1 tabulates the calculated structural parameters a , c/a , and $\varepsilon_1 = u - u_{\text{ideal}}$ for the III–V nitrides by three different groups [12–14]. In the case of Bernardini *et al.* [12], they optimized the structure within both the *generalized gradient*

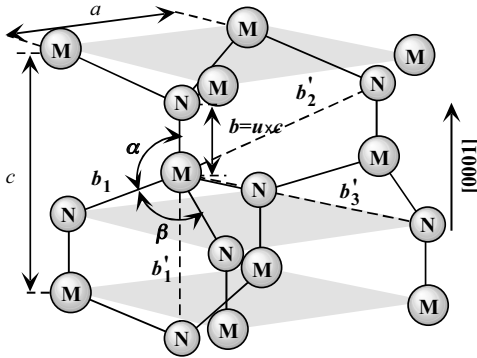


Figure 1.8 Schematic representation of a wurtzitic metal nitride structure with lattice constants a in the basal plane and c in the basal direction, u parameter, which is expressed as the bond length or the nearest neighbor distance (b) divided by c (0.375 in ideal crystal), α and β (109.47 in ideal crystal) are the bond angles, and b'_1 , b'_2 , and b'_3 , represent the three types of second nearest neighbor distances.

approximation (GGA) and *local density approximation* (LDA). The experimental data are from Leszczynski *et al.* [15].

In all Wz III nitrides, experimentally observed c/a ratios are smaller than ideal and it has been postulated that not being so would lead to the zinc blende phase [16]. There are two avenues that can lead to a deviation from ideal: changing the c/a ratio or changing the u value. It should be pointed out that a strong correlation exists between the c/a ratio and the u parameter so that when c/a decreases, the u parameter increases in a manner to keep the four tetrahedral distances nearly constant through a distortion of tetrahedral angles. For equal bond length to prevail, the following relation must hold:

$$u(1/3)(a^2/c^2) + 1/4. \quad (1.1)$$

Table 1.1 Structural parameters for GaN reported by Bechstedt, Großner, and Furthmüller (BGF) [13] and by Wei and Zunger (WZ) [14] using the local density approximation (LDA).

	a (Å)	c/a	ϵ_1 ($10^{-3}c/a$)
BGF	3.150	1.6310	6.5
WZ	3.189	1.6259	1.8
BFV (LDA)	3.131	1.6301	1.6
BFV (GGA)	3.197	1.6297	1.9
Experimental data	3.1890	1.6263	2.0

However, Bernardini, Fiorentini, and Vanderbilt [12] employed both the LDA and GGA methods. Lattice constant a is given in Å and ϵ_1 in $10^{-3}c/a$.

The nearest neighbor bond length along the c -direction (expressed as b in Figure 1.8) and off c -axis (expressed as b_1 in Figure 1.8) can be calculated as

$$b = cu \quad \text{and} \quad b_1 = \sqrt{\frac{1}{3}a^2 + \left(\frac{1}{2} - u\right)^2} c^2. \quad (1.2)$$

In addition to the nearest neighbors, there are three types of second nearest neighbors designated in Figure 1.8 as b'_1 (one along the c -direction), b'_2 (six of them), and b'_3 (three of them), which are given as [17]

$$b'_1 = c(1 - u), \quad b'_2 = \sqrt{a^2 + (uc)^2}, \quad \text{and} \quad b'_3 = \sqrt{\frac{4}{3}a^2 + c^2\left(\frac{1}{2} - u\right)^2}. \quad (1.3)$$

The bond angles, α and β , are given by [17]

$$\alpha = \pi/2 + \arccos \left[\left(\sqrt{1 + 3(c/a)^2(-u + 1/2)^2} \right)^{-1} \right], \quad (1.4)$$

$$\beta = 2 \arcsin \left[\left(\sqrt{4/3 + 4(c/a)^2(-u + 1/2)^2} \right)^{-1} \right].$$

Table 1.2 tabulates the calculated as well as experimentally observed structural parameters discussed above, inclusive of the lattice parameters, the nearest and second nearest neighbor distances, and the bond angles for three end binaries, GaN, AlN, and InN. The distances are in terms of Å.

The lattice parameters are commonly measured at room temperature by X-ray diffraction (XRD), which happens to be the most accurate one, using the Bragg law. In ternary compounds, the technique is also used for determining the composition; however, strain and relevant issues must be accounted for as the samples are in the

Table 1.2 Calculated (for ideal crystal) and experimentally observed structural parameters for GaN, AlN, and InN [17].

	GaN		AlN		InN	
	Ideal	Exp.	Ideal	Exp.	Ideal	Exp.
u	0.375	0.377	0.375	0.382	0.375	0.379
a (Å)	3.199	3.199	3.110	3.110	3.585	3.585
c/a	1.633	1.634	1.633	1.606	1.633	1.618
b (Å)	1.959	1.971	1.904	1.907	2.195	2.200
b_1 (Å)	1.959	1.955	1.904	1.890	2.195	2.185
b'_1 (Å)	3.265	3.255	3.174	3.087	3.659	3.600
b'_2 (Å)	3.751	3.757	3.646	3.648	4.204	4.206
b'_3 (Å)	3.751	3.749	3.646	3.648	4.204	4.198
α	109.47	109.17	109.47	108.19	109.47	108.69
β	109.47	109.78	109.47	110.73	109.47	110.24

form of epitaxial layers on foreign substrates. The accuracy of X-ray diffraction and less than accurate knowledge of the elastic parameters together allow determination of the composition to only within about 1% molar fraction. In addition to composition, the lattice parameter can be affected by free charge, impurities, stress (strain), and temperature [18]. Because the c/a ratio correlates with the difference of the electronegativities of the two constituents, components with the greatest differences show the largest departure from the ideal c/a ratio [19]. For GaN, the c/a ratio and the value of u are measured as 1.627 (1.634 in Ref. [17]) and 0.377, respectively, which are close to the ideal values [20]. AlN deviates significantly from the ideal parameters: $c/a = 1.601$ (1.606 in Ref. [17]) and $u = 0.382$. Although the data for InN are not as reliable, values of $u = 0.379$ and $c/a = 1.601$ have been reported [17]. Inhomogeneities, strain, partial relaxation of strain, and high concentration of structural defects may distort the lattice constants from their intrinsic values and cause a wide dispersion among the reported values. Table 1.3 lists a comparison of measured and calculated lattice parameters reported for AlN, GaN, and InN crystallized in the wurtzite structure in more detail in terms of the specifics of the sample used for measurements and complements. The dispersion is even a greater concern in ternary and quaternaries, as compositional inhomogeneities, in addition to the aforementioned issues, cause an additional dispersion. The particulars of the ternaries are discussed in Section 1.5.

The wurtzite polytypes of GaN, AlN, and InN form a continuous alloy system whose direct bandgaps range, according to data that adorned the literature for years, from 1.9 eV for InN, to 3.42 eV for GaN, and to 6.2 eV for AlN. A revisit of the InN bandgap indicates it to be about 0.78 eV [30] and the same for AlN is about 6 eV in which case the energy range covered would be about 0.7–6 eV. Thus, the III–V nitrides could potentially be fabricated into optical devices, which are active at wavelengths ranging from the red well to the ultraviolet. The bandgaps of nitrides,

Table 1.3 Measured and calculated lattice constants of wurtzite AlN, GaN, and InN.

Compound	Sample	a (Å)	c (Å)
AlN	Bulk crystal [21]	3.1106	4.9795
	Powder [22]	3.1130	4.9816
	Epitaxial layer on SiC [23]	3.110	4.980
	Pseudopotential LDA [24]	3.06	4.91
	FP-LMTO LDA [25]	3.084	4.948
GaN	Bulk crystal [18]	3.189	5.1864
	Relaxed layer on sapphire [26]	3.1892	5.1850
	Powder [29]	3.1893	5.1851
	Relaxed layer on sapphire [27]	3.1878	5.1854
	GaN substrate – LEO [28]	3.1896	5.1855
	Pseudopotential LDA [24]	3.162	5.142
	FP-LMTO LDA [25]	3.17	5.13
InN	Powder [29]	3.538	5.703
	Pseudopotential LDA [24]	3.501	5.669
	FP-LMTO LDA [25]	3.53	5.54

LDA: local density approximation; FP-LMTO: full-potential linear muffin-tin orbital.

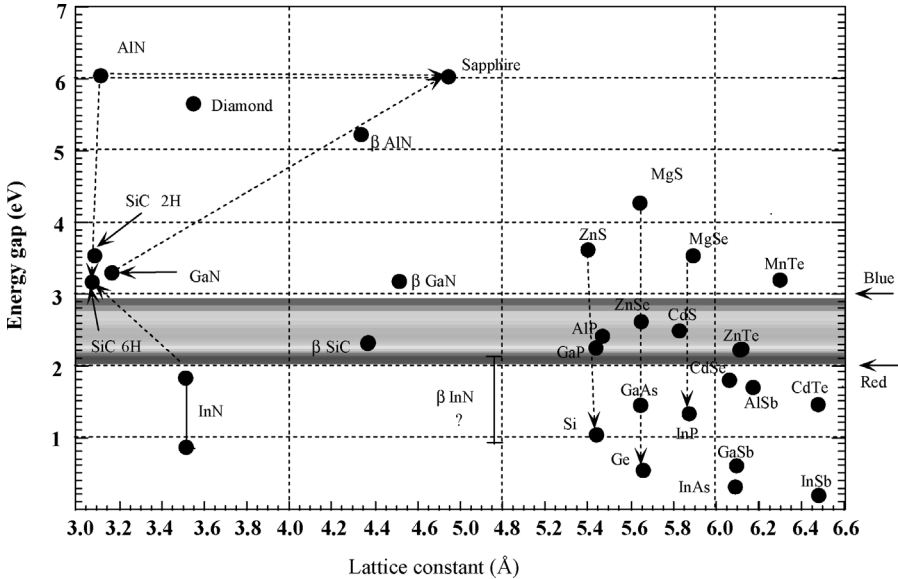


Figure 1.9 The bandgaps of nitrides, substrates commonly used for nitrides, and other conventional semiconductors versus their lattice constants. (Please find a color version of this figure on the color tables.)

substrates commonly used for nitrides, and other conventional semiconductors are shown in Figure 1.9 with respect to their lattice constants.

All III nitrides have partially covalent and partially ionic bonds. The concept of *fractional ionic character* (FIC) is useful in interpreting many physical phenomena in the crystals [31,32]. The FIC may be defined for a binary compound AB as $FIC = |Q_A^* - Q_B^*| / |Q_A^* + Q_B^*|$, where Q_A^* and Q_B^* are effective charges on atoms A and B. The FIC values range from zero for a covalent compound (each atom has four electrons) to 1 for an ionic compound (all eight electrons belong to the anion). Figure 1.10 displays the charge distribution along the AB bond for all three compounds. The arrow along the bond charge indicates the atomic boundaries in the crystals that are not always at the minimum of the line charge along the bond AB. This should be expected taking into account the partial covalent bond of the compounds, because only in the ionic crystals, the atomic boundary is clearly defined. Table 1.4 lists the calculated effective radii, r_{III} and r_N , the effective charges, and FIC for AlN, GaN, and InN. The ionicity of AlN is high. This may explain the difficulties with AlN doping. It is well known that only covalent semiconductors or semiconductors with a large covalent component can form hydrogen-like shallow levels in the bandgap by substitution of a host atom with a neighbor with one more or one less electron. GaN and InN have a smaller than AlN but nearly equal ionicity. GaN was doped both p- and n-type. Thus, one can expect that InN can also be doped n- and p-type. To date, only n-type InN has been obtained because of high volatility of nitrogen and easiness of nitrogen vacancy formation that acts as a donor in this compound.

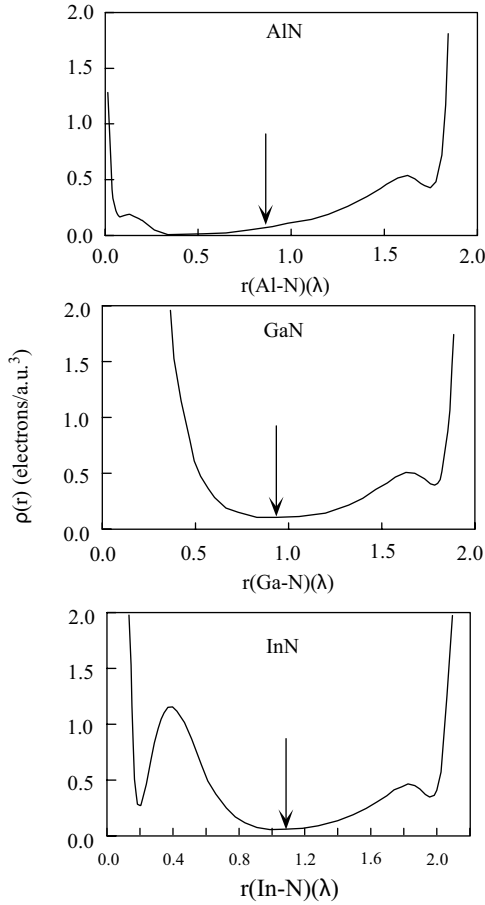


Figure 1.10 Charge density along the III-N bond in III nitride semiconductors.

The III-nitrides are commonly grown on mismatched substrates because of the lack of suitable native substrates. Thus, the epitaxial layers are strained during cool down, if they are sufficiently thick for them to relax at the growth temperature. The mechanical forces related to strain dramatically change the band structure of the epitaxial layers. The pressure dependence of the bandgap energy E_g can be expressed as $E_g = E_g(0) + gP + dP^2$, where $E_g(0)$ is the bandgap of stress-free semiconductor, g and d are the

Table 1.4 Calculated ionic radii (Å), effective charges (electrons), and the fractional ionic character (FIC) for III nitrides [32].

Compound	r_{III} (Å)	r_{N} (Å)	Q_{III}^* (e)	Q_{N}^* (e)	FIC
AlN	0.8505	1.0523	1.12	6.88	0.72
GaN	0.9340	1.0119	1.98	6.02	0.51
InN	1.0673	1.0673	1.83	6.17	0.54

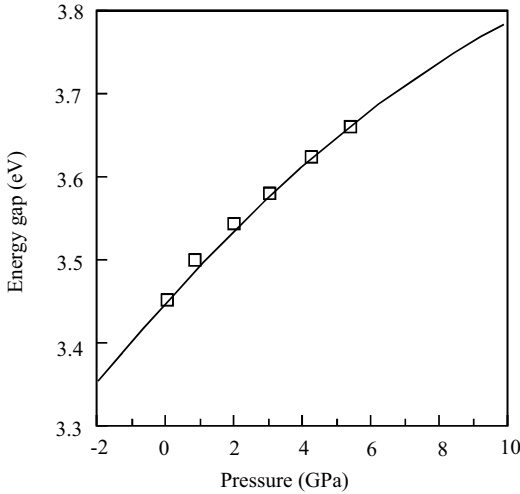


Figure 1.11 Pressure dependence of the GaN energy gap, showing the typical sublinear character. Solid line represents the calculations of Christiansen and Gorczyca [35], which have been rigidly upshifted by ~ 0.82 eV for a better fit with experiments, and the squares represent experimental results [6].

pressure coefficients, and P is the pressure. For GaN, g and d parameters are 4.2×10^{-3} and -1.8×10^{-5} , respectively [33,34]. The bandgap is in terms of eV and the pressure is in terms of kbar. The pressure dependence has, in general, a sublinear character. The variation of the GaN energy gap with pressure, both theoretical [35] and experimental [6], is shown in Figure 1.11. The calculated pressure coefficients for III nitrides are given in Table 1.5.

Parameters associated with mechanical properties of GaN in wurtzitic phase are tabulated in Tables 1.6 and 1.7, the latter dealing with the sound wave velocity. The same parameters for the zinc blende phase of GaN are tabulated in Tables 1.8 and 1.9.

Table 1.5 Calculated pressure coefficients for III nitrides including wurtzitic, zinc blende, and rock salt phases (g in units of meV GPa^{-1} and d in units of meV GPa^{-2}) [35].

Compound	Wurtzite polytype		Zinc blende polytype		Rock salt polytype	
	G	d	g	d	g	d
AlN	40	-0.32	42	-0.34	43	-0.18
GaN	39	-0.32	40	-0.38	39	-0.32
InN	33	-0.55	16	-0.02	41	-0.08

It should be noted that rock salt phases cannot be synthesized and exist only under high pressures beyond the phase transition point. g and d parameters with values of $E_g = E_g(0) + gP + dP^2$.

Table 1.6 Parameters related to mechanical properties of wurtzitic GaN (in part after Ref. [36]).

Wurtzite polytype GaN	Parameter value/comments	Comments/ references
Group of symmetry	C_{6v}^4 ($P6_3mc$)	
Molar volume, V_c ($\text{cm}^3 \text{mol}^{-1}$)	13.61	
Molecular mass (g mol^{-1})	83.7267	
Density (g cm^{-3})	6.11 or 6.15	The latter by Bougrov <i>et al.</i> [37]
Number of atoms in 1 cm^3	8.9×10^{22}	
Lattice constants	$a = 3.1893 \text{ \AA}$ for powder, $c = 5.1851 \text{ \AA}$ for powder ^a	
Bulk modulus B (GPa) (compressibility ⁻¹)	210 [38] ^b or $20.4 \times 10^{11} \text{ dyn cm}^{-2}$ (204 GPa)	The latter by Bougrov <i>et al.</i> [37]
dB/dP	4	
Young's modulus (GPa)	150	
Poisson's ratio, ν or σ_0 ($\nu = C_{13}/(C_{11} + C_{12})$)	0.23 ± 0.06 (0.198–0.37) from C parameters	[39]
Knoop's hardness (GPa)	15.5	At 300 K
Surface microhardness (kg mm^{-2})	1200–1700	300 K, using Knoop's pyramid test [36,40,41]
Nanoindentation hardness (GPa)	10.8 at 300 K	
Yield strength (GPa)	0.1 at 1000 K	
Deformation potential, E_{ds}	8.54 eV unscreened, 12 eV screened	
C_{11} (GPa)	390 ± 15 , $29.6 \times 10^{11} \text{ dyn cm}^{-2}$ (296 GPa)	[38,42]
C_{12} (GPa)	145 ± 20 , $13.0 \times 10^{11} \text{ dyn cm}^{-2}$ (130 GPa)	The second set is from Ref. [43]
C_{13} (GPa)	106 ± 20 , $15.8 \times 10^{11} \text{ dyn cm}^{-2}$ (158 GPa)	The second set is calculated from the mean square displacement of the lattice atoms measured by X-ray diffraction
C_{33} (GPa)	398 ± 20 , $26.7 \times 10^{11} \text{ dyn cm}^{-2}$ (267 GPa)	
C_{44} (GPa)	105 ± 10 , $2.41 \times 10^{11} \text{ dyn cm}^{-2}$ (241 GPa)	

$\nu(0001) = (\Delta a/a_{\text{relax}})/(\Delta c/c_{\text{relax}})$ or $\nu(0001) = (\Delta a/a_0)/(\Delta c/c_0)$ with $\Delta a = a_{\text{meas}} - a_{\text{relax}}$ and $\Delta c = c_{\text{meas}} - c_{\text{relax}}$. Conversion: $1 \text{ dyn cm}^{-2} = 0.1 \text{ Pa}$ (i.e., $1 \text{ GPa} = 10^{10} \text{ dyn cm}^{-2}$). For details of elastic constants and piezoelectric constants, see Tables 2.27 and 2.28, and at 300 K $B_s = 210 \pm 10 \text{ GPa}$, $B_s = [C_{33}(C_{11} + C_{12}) - 2(C_{13})^2]/[C_{11} + C_{12} + 2C_{33} - 4C_{13}]$.

^aSee Section 1.2.2 for details and lattice parameter for GaN on different substrates

^bAverage of Voigt and Reuss bulk modulus.

Table 1.7 Wave propagation properties in wurtzitic GaN [36].

Wave propagation direction	Wave character	Expression for wave velocity	Wave velocity (in units of 10^5 cm s^{-1})
[1 0 0]	V_L (longitudinal)	$(C_{11}/\rho)^{1/2}$	7.96
	V_T (transverse, polarization along [0 0 1])	$(C_{44}/\rho)^{1/2}$	4.13
	V_T (transverse, polarization along [0 1 0])	$(C_{11} - C_{12})/2\rho)^{1/2}$	6.31
[0 0 1]	V_L (longitudinal)	$(C_{33}/\rho)^{1/2}$	8.04
	V_T (transverse)	$(C_{44}/\rho)^{1/2}$	4.13

Parameters associated with thermal properties of GaN in wurtzitic and zinc blende phases (expected to be identical or nearly identical – treated to be identical here) are tabulated in Table 1.10.

The parameters associated with electrical and optical properties of wurtzitic GaN are tabulated in Table 1.11. The same parameters associated with the zinc blende phase of GaN are tabulated in Table 1.12.

Table 1.8 Parameters related to mechanical properties of zinc blende GaN (in part after Ref. [36]).

Zinc blende polytype GaN	Parameter value/comments	Comments/references
Group of symmetry	$T_d^2(F43m)$	
Molar volume, V_c , v_a , or Ω ($\text{cm}^3 \text{ mol}^{-1}$)	$(\sqrt{3}a^2c)/4 = 2.283 \times 10^{-23} \text{ cm}^3$	
Molecular mass (g mol^{-1})	1.936×10^{-23}	
Density (g cm^{-3})	6.15	
Number of atoms in 1 cm^3	8.9×10^{22}	
Lattice constant (\AA)	$a = 4.511 - 4.52$	
Bulk modulus, B (GPa)	$B_s = 204$ [36], 201 (theory) [45], 237 [46], 200 [47]	$B_s = \frac{C_{33}(C_{11} + C_{12}) - 2(C_{13})^2}{C_{11} + C_{12} + 2C_{33} - 4C_{13}}$
dB/dP	3.9, 4.3	
Young's modulus (GPa)	181 [36]	$Y_0 = (C_{11} + 2C_{12}) / (C_{11} - C_{12}) / (C_{11} + C_{12})$
Shear modulus, C' (GPa)	67 [36]	$C' = (C_{11} - C_{12})/2$
Poisson's ratio, ν or σ_0	0.352 [36]	ν or $\sigma_0 = C_{13} / (C_{11} + C_{12})$
Knoop's hardness		
Surface microhardness		
Nanoindentation hardness		
Yield strength		
Deformation potential, E_{ds}		
C_{11} (GPa)	293	[42]
C_{12} (GPa)	159	
C_{44} (GPa)	155	

$$B_s = [C_{33}(C_{11} + C_{12}) - 2(C_{13})^2] / [C_{11} + C_{12} + 2C_{33} - 4C_{13}] \text{ or } B_s = \frac{C_{33}(C_{11} + C_{12}) - 2(C_{13})^2}{C_{11} + C_{12} + 2C_{33} - 4C_{13}}$$

Table 1.9 Wave propagation properties in zinc blende GaN (after Ref. [36]).

Wave propagation direction	Wave character	Expression for wave velocity	Wave velocity (in units of 10^5 cm s^{-1})
[1 0 0]	V_L (longitudinal)	$(C_{11}/\rho)^{1/2}$	6.9
	V_T (transverse)	$(C_{44}/\rho)^{1/2}$	5.02
[1 1 0]	V_L (longitudinal)	$[(C_{11}+C_{12}+2C_{44})/2\rho]^{1/2}$	7.87
	$V_{//}$ (transverse)	$V_{//} = V_T = (C_{44}/\rho)^{1/2}$	5.02
	V_{\perp} (transverse)	$[(C_{11} - C_{12})/2\rho]^{1/2}$	3.3
[1 1 1]	V'_1	$[(C_{11} + 2C_{12} + 4C_{44})/3\rho]^{1/2}$	8.17
	V''_1	$[(C_{11} - C_{12} + C_{44})/3\rho]^{1/2}$	3.96

For the crystallographic directions, see Ref. [44].

Table 1.10 Parameters related to thermal properties of GaN, wurtzitic, and zinc blende phases are expected to be the in this respect with the exception of the first two parameters, which are for the wurtzitic phase (in part Ref. [36]).

GaN	Parameter value/comments	Comments/references
Temperature coefficient (eV K^{-1})	$dE_g/dT = -6.0 \times 10^{-4}$	Wurtzite structure only
Thermal expansion (K^{-1})	$\Delta a/a = 5.59 \times 10^{-6}$, $\alpha_{ } = \alpha_a$ $= 5.59 \times 10^{-6}$ (wurtzite structure) [48]	$\Delta c/c = 3.17 \times 10^{-6}$; for a plot versus temperature, see Ref. [49] (wurtzite structure only)
Thermal conductivity κ ($\text{W cm}^{-1} \text{K}^{-1}$)	11.9 at 77 K, 2.3 at 300 K, 1.5 at 400 K	For low dissociation material ($\leq 10^6 \text{ cm}^{-2}$)
Debye temperature (K)	600	
Melting point ($^\circ\text{C}$)	>1700 (at 2 kbar), 2500 (at tens of kbar)	[50]
Specific heat ($\text{J g}^{-1} \text{ }^\circ\text{C}^{-1}$)	0.49	[37]
Thermal diffusivity ($\text{cm}^2 \text{ s}^{-1}$)	0.43	[37]
Heat of formation, ΔH_{298} (kcal mol^{-1})	-26.4	
Heat of atomization, ΔH_{298} (kcal mol^{-1})	-203	
Heat of sublimation (kcal mol^{-1})	72.4 ± 0.5	
Heat capacity ($\text{J mol}^{-1} \text{K}^{-1}$)	35.4 at 300 K	
Specific heat ($\text{J mol}^{-1} \text{K}^{-1}$) ($298 \text{ K} < T < 1773 \text{ K}$)	$C_p = 38.1 + 8.96 \times 10^{-3}T$	[51]
Enthalpy, ΔH^0 (kcal mol^{-1})	-37.7	
Standard entropy of formation, ΔS^0 ($\text{cal mol}^{-1} \text{K}^{-1}$)	-32.43	

The specific heat C_p of Wz GaN at constant pressure for $298 \text{ K} < T < 1773 \text{ K}$ is $C_p = 38.1 + 8.96 \times 10^{-3}T$ ($\text{J mol}^{-1} \text{K}^{-1}$) [51].

Table 1.11 Parameters related to electrical and optical properties of Wz GaN (in part after Refs [36,44]).

Wurtzite polytype GaN	Parameter value/comments	Comments/ references		
Bandgap energy, E_g (eV), direct	3.42 at 300 K, 3.505 at 1.6 K			
Breakdown field (cm^{-1})	$3\text{--}5 \times 10^6$ at 300 K			[53]
Electron affinity (eV)	4.1			[37]
Energy separation between Γ and M-L valleys (eV)	-1.9 at 300 K			[37]
	1 at 300 K			[52]
Energy separation between M-L valleys degeneracy (eV)	0.6 at 300 K			[37]
	0.6 at 300 K			[52]
Energy separation between Γ and A valleys (eV)	1.3–2.1 at 300 K			[37]
	2 at 300 K			[52]
Energy separation between A valley degeneracy (eV)	1 at 300 K			[37]
Index of refraction	0.2 at 300 K n (1 eV) = 2.35 or 2.3 2.29, n (3.42 eV) = 2.85 at 300 K (extrapolated to 0 eV), $E \perp c$ interference method (the value for $E \parallel c$ is 1.5(2)% lower at 500 nm); also see energy dependence and long-wavelength value [54]			[52]
Dielectric constants (static)	10.4 ($E \parallel c$) 9.5 ($E \perp c$)			[55] [55]
Dielectric constants (high frequency)	8.9 in c -direction ($E \parallel c$) at 300 K 5.35 5.8 ($E \parallel c$) at 300 K 5.35 ($E \perp c$) at 300 K 5.47 ($E \parallel c$)			[37] [37] [56] [55]
Optical LO phonon ener- gy (meV)	91.2			[37]
A_1 -LO, $\nu_{A_1}(\text{LO})$ (cm^{-1})	710–735	[57]	744	Reflectivity [55]
A_1 -TO, $\nu_{A_1}(\text{TO} \parallel)$ (cm^{-1})	533–534	[34]	533	Raman [56]
E_1 -LO, $\nu_{E_1}(\text{LO} \perp)$ (cm^{-1})	741–742	[58]	746	Reflectivity [55]
E_1 -TO, $\nu_{E_1}(\text{TO} \perp)$ (cm^{-1})	556–559	[59]	559	Raman [60]
E_2 (low) (cm^{-1})	143–146			
E_2 (high) (cm^{-1})	560–579			

Table 1.11 (Continued)

Wurtzite polytype GaN	Parameter value/comments	Comments/ references
Energy of spin-orbital splitting, E_{so} (meV)	11 (+5, -2) at 300 K calculated from the values of energy gap $E_{g,dir}$ (given in this table)	[61]
Energy of crystal-field splitting, E_{cr} (meV)	40 at 300 K	[37]
	22 (2), calculated from the values of energy gap $E_{g,dir}$ (given in this table)	[61]
Effective electron mass, m_e or m_e^{\parallel}	0.20 m_0 at 300 K	[37]
	0.20 m_0	[62]
	0.27 m_0 by Faraday rotation	[52]
	0.138–0.2	
Effective electron mass, $m_{e\perp}$ or m_e^{\perp}	0.20 m_0 , 300 K; fit of reflectance spectrum	[63]
	0.15–0.23 m_0	[52]
Effective hole mass	0.8 m_0 at 300 K	[64]
Effective hole masses (heavy), m_{hh}	$m_{hh} = 1.4m_0$ at 300 K	Calculated
	$m_{hhz} = m_{hh}^{\parallel} = 1.1m_0$ at 300 K	[15]
	$m_{hh\perp} = m_{hh}^{\perp} = 1.6m_0$ at 300 K	[70]
	$m_{hh}^{\parallel} = 1.1 - 2.007m_0$	[52]
	$m_{hh}^{\perp} = 1.61 - 2.255m_0$	[52]
Effective hole masses (light)	$m_{lh} = 0.3m_0$ at 300 K	Calculated
	$m_{lhz} = m_{lh}^{\parallel} = 1.1m_0$ at 300 K	[15]
	$m_{lh\perp} = m_{lh}^{\perp} = 0.15m_0$ at 300 K	[70]
	$m_{lh}^{\parallel} = 1.1 - 2.007m_0$	[52]
	$m_{lh\perp} = 0.14 - 0.261m_0$	[52]
Effective hole masses (split-off band), m_s	$m_{sh} = 0.6m_0$ at 300 K	Calculated
	$m_{shz} = m_{sh}^{\parallel} = 0.15m_0$ at 300 K	[36]
	$m_{sh\perp} = m_{sh}^{\perp} = 1.1m_0$ at 300 K	[70]
	$m_{sh\perp} = m_{sh}^{\parallel} = 0.12 - 0.16m_0$	[52]
	$m_{ch}^{\perp} = 0.252 - 1.96m_0$	[52]
Effective mass of density of state, m_v	1.4 m_0	[37]
Effective conduction band density of states (cm^{-3})	2.3×10^{18} at 300 K	
Effective valence band density of states (cm^{-3})	4.6×10^{19} at 300 K	
Electron mobility ($\text{cm}^2 \text{V}^{-1} \text{s}^{-1}$)	~1400 experimental at 300 K	50 000 at 20 K [65]
Hole mobility ($\text{cm}^2 \text{V}^{-1} \text{s}^{-1}$)	<20	At 300 K
n-doping range (cm^{-3})	10^{16} cm^{-3} –high 10^{19}	

(Continued)

Table 1.11 (Continued)

Wurtzite polytype GaN	Parameter value/comments	Comments/ references
p-doping range (cm ⁻³)	10 ¹⁶ cm ⁻³ –mid 10 ¹⁸	
Diffusion coefficient for electrons (cm ² s ⁻¹)	25	[36]
Diffusion coefficient for holes (cm ² s ⁻¹)	5, 26, 94	[36,53]

The details of the energies of high symmetry points compiled by Fritsch *et al.* [52] are given in Table 2.1. Dependence of the bandgap on hydrostatic pressure: $E_g = E_g(0) + gP + dP^2$, where $E_g(0)$ is the bandgap of stress-free GaN. The values for g parameter are 39–42 meV GPa⁻¹ and the same for d parameter are -0.18 to -0.32 meV GPa⁻². For others, see Table 1.5.

The phonon energies are discussed later on in Table 1.27 in detail and effective masses are discussed in Chapter 2. More details of effective masses can be found in Table 2.9.

More should be said about the dielectric constants. Electromagnetic theory indicates that for any longitudinal electromagnetic wave to propagate, the dielectric function $\epsilon(\omega)$ must vanish. Doing so leads to [66]

$$\frac{\epsilon(\omega)}{\epsilon(\infty)} = \frac{\omega_{\text{LO}}^2 - \omega^2}{\omega_{\text{TO}}^2 - \omega^2}, \quad (1.5)$$

where ω_{LO} and ω_{TO} represent the transverse optical (TO) and longitudinal optical (LO) phonon frequencies and $\epsilon(\omega)$ and $\epsilon(\infty)$ represent the low and high (optical) frequency dielectric constants. The phonon branches associated with a wurtzitic symmetry are discussed in Section 1.2.2 dealing with the mechanical properties of GaN. When $\omega = \omega_{\text{LO}}$, the dielectric function vanishes, $\epsilon(\omega_{\text{LO}}) = 0$. Equation 1.5 can be expanded to the directional dependence of the dielectric function in nitrides in general and GaN in particular. In the direction parallel to the c -axis or the z -direction, from the Γ point to the A point, in the k -space, (with x, y representing the in-plane coordinates), the low- and high-frequency dielectric functions are related each with the help of $A_1(\text{LO})$ and $E_1(\text{TO})$ phonons through [67]

$$\epsilon_{//}(\omega) = \epsilon_{\perp}^{\infty} \frac{\omega^2 - \omega_{//}^2(\text{LO})}{\omega^2 - \omega_{//}^2(\text{TO})}. \quad (1.6)$$

Likewise, Equation 1.5 can be expanded in the direction perpendicular to the c -axis or in the basal plane or the (x, y) plane, the z -direction (in k -space between the Γ point and $M(1/2, 0, 0)$ or $K(1/3, 1/3, 0)$ points), the low- and high-frequency dielectric functions are related each with the help of $A_1(\text{TO})$ and $E_1(\text{LO})$ phonons through

$$\epsilon_{\perp}(\omega) = \epsilon_{\perp}^{\infty} \frac{\omega^2 - \omega_{\perp}^2(\text{LO})}{\omega^2 - \omega_{\perp}^2(\text{TO})}, \quad (1.7)$$

where \perp and $//$ indicate in the basal plane and along the c -direction, respectively.

Table 1.12 Parameters related to electrical and optical properties of zinc blende GaN (in part after Refs [36,44]).

Zinc blende polytype GaN	Parameter/comments	Comments/references
Bandgap energy (eV)	3.2–3.28 at 300 K	3.302 at low temperature
Breakdown field (V cm^{-1})	$\sim 5 \times 10^6$	[36]
Index of refraction	n (at 3 eV) = 2.9, 2.3	
Dielectric constant (static)	9.7 at 300 K 9.2 by $(2\epsilon_0^\perp + \epsilon_0^\parallel)/3$ of wurtzitic form	[37] [52]
Dielectric constant (high frequency)	5.3 at 300 K	Using Lyddane–Sachs–Teller relation ($\epsilon_0/\epsilon_{\text{high}} = \omega_{\text{LO}}^2/\omega_{\text{TO}}^2$)
Energy separation between Γ and X valleys, E_{Γ} (eV)	1.4 ~ 1.1	[36] [52]
Energy separation between Γ and L valleys, E_{L} (eV)	1.6–1.9 ~ 2	[36] [52]
Spin–orbit splitting in valence band, Δ_{so} or E_{so} (eV)	0.02 0.017	At 300 K [36] [69]
Effective electron mass, m_e	$0.13m_0$ $0.14m_0$	At 300 K [37] [52]
Effective hole masses (heavy)	$m_{\text{hh}} = 1.3m_0$, $m_{\text{hh}}^{[110]} = 1.52m_0$, $m_{\text{hh}}^{[100]} = 0.8m_0$, $m_{\text{hh}}^{[100]} = 0.84m_0$, $m_{\text{hh}}^{[111]} = 1.7m_0$, $m_{\text{hh}}^{[111]} = 2.07m_0$	At 300 K [36,70] Second set of figures are from Ref. [52], which are deemed more reliable
Effective hole masses (light)	$m_{\text{lh}} = 0.19m_0$, $m_{\text{lh}}^{[110]} = 0.20m_0$, $m_{\text{lh}}^{[100]} = 0.21m_0$, $m_{\text{lh}}^{[100]} = 0.22m_0$, $m_{\text{lh}}^{[111]} = 0.18m_0$, $m_{\text{lh}}^{[111]} = 0.19m_0$	
Effective hole masses (split-off band), m_s , m_{ch} , or m_{so}	$m_{\text{sh}} = 0.33m_0$, $m_{\text{so}} = 0.35m_0$, $m_{\text{hh}}^{[100]} = 0.33m_0$, $m_{\text{hh}}^{[111]} = 0.33m_0$	
Effective conduction band density of states	$1.2 \times 10^{18} \text{ cm}^{-3}$	At 300 K [37]
Effective valence band density of states	$4.1 \times 10^{19} \text{ cm}^{-3}$	At 300 K [37]
Electron mobility ($\text{cm}^2 \text{ V}^{-1} \text{ s}^{-1}$)	≤ 1000 at 300 K	[36]
Hole mobility ($\text{cm}^2 \text{ V}^{-1} \text{ s}^{-1}$)	≤ 350 at 300 K	[36]
Diffusion coefficient for electrons ($\text{cm}^2 \text{ s}^{-1}$)	25	[36]
Diffusion coefficient for holes ($\text{cm}^2 \text{ s}^{-1}$)	9, 9.5, 32	[36]
Electron affinity	4.1 eV	[37]
Optical LO phonon energy (meV)	87.3	At 300 K

The details of the energies of high symmetry points are given in Table 2.1.

For wurtzitic GaN, the various directional components of phonon frequencies are $\omega_{\perp}(\text{LO}) \rightarrow E_1(\text{LO}) = 91.8 \text{ meV}$, $\omega_z(\text{LO}) = \omega_{//}(\text{LO}) \rightarrow A_1(\text{LO}) = 91 \text{ meV}$, $\omega_{\perp}(\text{TO}) \rightarrow E_1(\text{TO}) = 69.3 \text{ meV}$, and $\omega_z(\text{TO}) = \omega_{//}(\text{TO}) \rightarrow A_1(\text{TO}) = 66 \text{ meV}$. In the z -direction (along the c -direction) and perpendicular to the z -direction (in basal plane), LO and TO phonons are not mixed. For any direction other than the in-plane and out-of-plane configurations, the LO and TO phonons mix and hybridize. For a given propagation direction with an angle θ relative to the c -axis ($0z$), one finds three phonon branches. One is an ordinary TO phonon mode with atomic displacement in the $(0xy)$ plane. The other two branches have a mixed TO and LO character and their dielectric functions are given by the solutions of [68]

$$\varepsilon_{//} \cos^2 \theta + \varepsilon_{\perp} \sin^2 \theta = 0. \quad (1.8)$$

Using the above relationship, the phonon energy as a function of the angle can easily be calculated. Doing so leads to the conclusion that the upper branch (LO-like) remains between $A_1(\text{LO})$ and $E_1(\text{LO})$ energies, whereas the lower branch (TO-like) remains between $A_1(\text{TO})$ and $E_1(\text{TO})$ energies. Therefore, the dispersion remains small compared to the LO–TO separation, owing to the relatively small cell asymmetry and the large ionicity of atomic bonds. A more important consequence of LO–TO mixing is that the TO-like mode becomes coupled to carriers whereas in the c -direction $A_1(\text{LO})$ mode and in the basal plane $E_1(\text{LO})$ phonons couple to the carriers.

For the special case $\omega = 0$ (or very small frequencies compared to the LO and TO phonon frequencies), the relationship between the optical and static dielectric constants reduces to the well-known *Lyddane–Sach–Teller* relationship

$$\frac{\varepsilon(\omega)}{\varepsilon(\infty)} = \frac{\omega_{\text{LO}}^2}{\omega_{\text{TO}}^2}, \quad (1.9)$$

which will be used to determine the optical frequency dielectric constant from the knowledge of $A_1(\text{LO})$ and $A_1(\text{TO})$ phonon frequencies along the c -direction and $E_1(\text{LO})$ and $E_1(\text{TO})$ in the basal plane. This relationship is used very often.

Parameters related to the energy bandgap, carrier mass, and mechanical properties of AlN have been determined [71–76]. Extensive data on all the binary and ternary band structure parameters can be found in Chapter 2. For example, additional parameters on the critical point energies for Wz GaN, AlN, and InN are given in Tables 2.1–2.3, respectively. Tables 2.4–2.6 list the critical point energies for ZB GaN, AlN, and InN, respectively. Effective masses and other band parameters for Wz GaN are listed in Table 2.9. Table 2.10 tabulates the Luttinger band parameters for ZB GaN. Table 2.14 lists the effective band parameters for Wz AlN, whereas the effective masses and band parameters for Wz AlN are tabulated in Table 2.15. Luttinger parameters for ZB AlN are listed in Table 2.16. The band parameters and effective masses for Wz InN are tabulated in Tables 2.19 and 1.20, respectively.

Returning to the content of this chapter, parameters associated with the mechanical properties of AlN in wurtzitic and zinc blende phases are tabulated in Tables 1.13 and 1.14, respectively. The parameters related to the sound wave velocity in wurtzitic AlN are listed in Table 1.15.

Table 1.13 Parameters related to mechanical properties of wurtzitic AlN (in part after Ref. [36]).

Wurtzite AlN	Parameter/comments	Comments/references
Group of symmetry	C_{6v}^4 ($P6_3mc$)	
Number of atoms in 1 cm^3	9.58×10^{22}	
Molar volume, V_c ($\text{cm}^3 \text{ mol}^{-1}$)	12.47	
Molecular mass (g mol^{-1})	40.9882	
Density (g cm^{-3})	3.28	
	3.255 g cm^{-3} by X-ray	[77]
	3.23 g cm^{-3} by X-ray	[78]
Lattice constants	$a = 3.112 \text{ \AA}$, $c = 4.979\text{--}4.982 \text{ \AA}$	
Bulk modulus, B (GPa)	159.9–210.1, $21 \times 10^{11} \text{ dyn cm}^{-2}$	[78]
	(210 GPa) ($B_s = 210$)	
dB/dP	5.2–6.3	
Young's modulus, E or Y_0 (GPa)	374, 308	The latter from Ref. [79]
Poisson's ratio, ν or σ_0	0.18–0.21	
Poisson's ratio σ_0 along the different crystallographic directions	$\{0001\}$, c -plane $\{11\bar{2}0\}$, a -plane ($l = \langle 0001 \rangle$, $m = \langle 1\bar{1}00 \rangle$) $\{11\bar{2}0\}$, a -plane ($l = \langle 1\bar{1}00 \rangle$, $m = \langle 0001 \rangle$)	0.287 Ref. [80] 0 Ref. [80] 0.216 Ref. [80]
Knoop's hardness (GPa)	10–14 at 300 K	[81]
Nanoindentation hardness (GPa)	18	[82]
Yield strength (GPa)	0.3 at 1000 °C	
Surface microhardness on basal plane (0001)	800 kg mm^{-2} by 300 K, using Knoop's pyramid test	[36,40,41]
C_{11} (GPa) ^a	410 ± 10	[42,83]
C_{12} (GPa) ^a	149 ± 10	Refer to Table 1.29 as well
C_{13} (GPa) ^a	99 ± 4	Refer to Table 1.29 as well
C_{33} (GPa) ^a	389 ± 10	Refer to Table 1.29 as well
C_{44} (GPa) ^a	125 ± 5	Refer to Table 1.29 as well
Velocity of the longitudinal sound waves, v_l	$10\,127 \text{ m s}^{-1}$	[79]
Velocity of the shear waves, v_s	6333 m s^{-1}	The sound velocities and related elastic module (experimental data)
Longitudinal elastic modulus, C_l	334 GPa	
Shear elastic modulus, C_s	131 GPa	

Conversion: $1 \text{ dyn cm}^{-2} = 0.1 \text{ Pa}$ (i.e., $1 \text{ GPa} = 10^{10} \text{ dyn cm}^{-2}$). See Table 1.29 for more details. For details of elastic constants and piezoelectric constants, see Tables 2.27 and 2.28. This expression is given already in conjunction with Table 1.6 and it is also $B_s = [C_{33}(C_{11} + C_{12}) - 2(C_{13})^2]/[C_{11} + C_{12} + 2C_{33} - 4C_{13}]$. Temperature derivatives of the elastic module: $\text{dln } C_l/\text{dT} = -0.37 \times 10^{-4} \text{ K}^{-1}$; $\text{dln } C_s/\text{dT} = -0.57 \times 10^{-4} \text{ K}^{-1}$; $\text{dln } B_s/\text{dT} = -0.43 \times 10^{-4} \text{ K}^{-1}$.

^aSee Table 1.29 for a more in-depth treatment of these parameters.

Parameters associated with thermal properties of wurtzitic AlN are tabulated in Table 1.16.

Parameters associated with electrical and optical properties of wurtzitic AlN are tabulated in Table 1.17. The same range of parameters associated with the zinc blende

Table 1.14 Parameters related to mechanical properties of zinc blende AlN.

Zinc blende AlN	Not much is known about the zinc blende phase		Comments/references
Lattice constant (Å)	$a = 4.38$		
Bandgap (eV)	5.4, indirect		[84]
E_g^x (eV)	4.9		[84]
E_g^z (eV)	9.3		[84]
Bulk modulus, B (GPa)	228		$B_s = (C_{11} + 2C_{12})/3$
Young's modulus (GPa)			$Y_0 = (C_{11} + 2C_{12}) \times$ $(C_{11} - C_{12}) / (C_{11} + C_{12})$
Shear modulus (GPa)			$C' = (C_{11} - C_{12})/2$
Poisson's ratio, ν or σ_0			ν or $\sigma_0 = C_{12} / (C_{11} + C_{12})$
C_{11} (GPa)	348	304	The latter figures are from Ref. [84]
C_{12} (GPa)	168	160	
C_{44} (GPa)	135	193	
m_e^* (Γ)	0.25		[84]
m_x^* (X)	0.53		[84]
m_x^* (X)	0.31		[84]

See Table 2.18 for more details.

phase of GaN is tabulated in Table 1.18. Mechanical, phonon, properties of *epitaxial* AlN (deposited on silicon and sapphire substrates at ~ 325 K by ion beam assisted deposition (IBAD)) have been investigated by Ribeiro *et al.* Raman scattering measurements revealed interesting features related to the atomic composition and structure of the films [94]. Vibrational modes corresponding to 2TA(L) at ~ 230 cm^{-1} , 2TA(X) at ~ 304 cm^{-1} , 2TA(Σ) at ~ 435 cm^{-1} , TO(Γ) at 520 cm^{-1} , TA(Σ) + TO(Σ) at ~ 615 cm^{-1} , accidental critical points at ~ 670 and ~ 825 cm^{-1} , 2TO(Δ) at ~ 950 cm^{-1} , 2TO(L) at ~ 980 cm^{-1} , 2TO(Γ) at ~ 1085 cm^{-1} , 2TA(X) + 2TO(Γ) at ~ 1300 cm^{-1} , and 3TO(Γ) at ~ 1450 cm^{-1} have been observed. While identifying the vibrational modes, one should be wary of the peak at ~ 2330 cm^{-1} caused by the molecular nitrogen on

Table 1.15 Acoustic wave propagation properties in wurtzite AlN [36].

Wave propagation direction	Wave character	Expression for wave velocity	Wave velocity (in units of 10^5 cm s^{-1})
[1 0 0]	V_L (longitudinal)	$(C_{11}/\rho)^{1/2}$	11.27
	V_T (transverse, polarization along [0 0 1])	$(C_{44}/\rho)^{1/2}$	6.22
	V_T (transverse, polarization along [0 1 0])	$(C_{11}-C_{12})/2\rho)^{1/2}$	6.36
[0 0 1]	V_L (longitudinal)	$(C_{33}/\rho)^{1/2}$	10.97
	V_T (transverse)	$(C_{44}/\rho)^{1/2}$	6.22

For the crystallographic directions, see Ref. [44].

Table 1.16 Parameters related to thermal properties of wurtzitic AlN (in part after Ref. [36]).

Wurtzite polytype AlN	Value	Comments/references
Thermal expansion (K^{-1})	$\Delta a/a = \alpha_{ } = \alpha_a = 4.2 \times 10^{-6}$, $\Delta c/c = \alpha_{ort} = \alpha_c = 5.3 \times 10^{-6}$ $\Delta a/a = 2.9 \times 10^{-6}$, $\Delta c/c = 3.4 \times 10^{-6}$ $\alpha_{ort} = \alpha_c = 5.27 \times 10^{-6}$, $\alpha_{ } = \alpha_a = 4.15 \times 10^{-6}$	[48,85–87] [88] $T = 20\text{--}800^\circ\text{C}$. X-ray, epitaxial layers, by Sirota and Golodushko [89], also see Ref. [48] [90]; later results by Slack <i>et al.</i> [91]
Thermal conductivity ($\text{W cm}^{-1} \text{K}^{-1}$)	$\kappa = 2.85\text{--}3.2$	[90]; later results by Slack <i>et al.</i> [91]
Thermal diffusivity ($\text{W cm}^{-1} \text{ }^\circ\text{C}^{-1}$)	2.85 at 300 K	[90]
Debye temperature (K)	950, 1150	
Melting point (K)	3273 3023 (between 100 and 500 atm of nitrogen) 3487 (2400 $^\circ\text{C}$ at 30 bar)	[92] [78]
Specific heat ($\text{J g}^{-1} \text{ }^\circ\text{C}^{-1}$)	0.6	See Figure 1.29 and the expressions below this table
Thermal diffusivity ($\text{cm}^2 \text{ s}^{-1}$)	1.47	
Heat of formation, ΔH_{298} (kcal mol^{-1})	−64	
Heat of atomization, ΔH_{298} (kcal mol^{-1})	−209.7	
Free energy, ΔG_{298} (kcal mol^{-1})	−68.15	

For $293 < T < 1700 \text{ K}$, $\Delta a/a_{300} = -8.679 \times 10^{-2} + 1.929 \times 10^{-4}T + 3.400 \times 10^{-7}T^2 - 7.969 \times 10^{-11}T^3$. For $293 < T < 1700 \text{ K}$, $\Delta c/c_{300} = -7.006 \times 10^{-2} + 1.583 \times 10^{-4}T + 2.719 \times 10^{-7}T^2 - 5.834 \times 10^{-11}T^3$. The specific heat C_p of AlN for constant pressure: for $300 < T < 1800 \text{ K}$, $C_p = 45.94 + 3.347 \times 10^{-3}T - 14.98 \times 10^5 T^{-2}$ ($\text{J mol}^{-1} \text{ K}^{-1}$); for $1800 < T < 2700 \text{ K}$, $C_p = 37.34 + 7.866 \times 10^{-3}T$ ($\text{J mol}^{-1} \text{ K}^{-1}$). After Ref. [93]. Optical emission measurements indicate the FX_A transition at 6.023 with an associated binding energy of 63 meV, which sets the bandgap of Wz AlN at 6.086.

the surface of c-Si [95]. It is worth noting that, owing to the extremely weak Raman signal usually presented by AlN films, it is not uncommon to ascribe some of the features erroneously to AlN [96].

Conduction band first- and second-order pressure derivatives [36]:

$$\begin{aligned}
 E_g &= E_g(0) + 3.6 \times 10^{-3}P - 1.7 \times 10^{-6}P^2 \text{ (eV)} & [121] \\
 E_M &= E_M(0) + 7.5 \times 10^{-4}P + 1.0 \times 10^{-6}P^2 \text{ (eV)} \\
 E_L &= E_L(0) + 8.0 \times 10^{-4}P + 6.9 \times 10^{-7}P^2 \text{ (eV)} \\
 E_k &= E_k(0) + 6.3 \times 10^{-4}P + 1.7 \times 10^{-6}P^2 \text{ (eV)}
 \end{aligned}$$

where P is pressure in kbar.

Table 1.17 Parameters related to optical and electrical properties of wurtzitic AlN [97–102] (in part from Ref. [36]).

Wurtzite polytype AlN	Parameter	Comments/references
Bandgap energy (eV) From the dichroism of the absorption edge, it follows that the $\Gamma_{1'}$ state lies slightly above the Γ_6 state (transition $E c$ ($\Gamma_{1'v} - \Gamma_{1c}$) at lower energy than transition $E \perp c$ ($\Gamma_{6v} - \Gamma_{1c}$)), both states being split by crystal field interaction [105]	6.026 at 300 K	[103,104]
	6.2 eV at 300 K	Excitonic contribution near direct edge [105]
	6.23 at 77 K	Excitonic contribution near direct edge [105]
	6.28 at 300 K	Excitonic edge assuming exciton binding energy of 75 meV [106]
	6.086 at 5 K	With a free exciton binding energy of 63 meV [107,108]
Breakdown field (V cm^{-1}) dE_g/dP (eV bar^{-1})	~ 6.0 at 300 K	
	~ 6.1 at 5 K	
Conduction band energy separation between Γ and M–L valleys (eV)	$1.2\text{--}1.8 \times 10^6$ 3.6×10^{-3}	[36] [109,110]
Conduction band energy separation between Γ and M–L valleys (eV)	~ 0.7 ~ 1	[78] [52]
Conduction band energy separation between Γ and M–L valleys (eV)	0.6	[78]
Conduction band energy separation between M–L valleys degeneracy (eV)	~ 0.2	[52]
Conduction band energy separation between Γ and K valleys (eV)	~ 1.0	[78]
Conduction band K valley degeneracy (eV)	~ 0.7 2	[52] [78]; empirical pseudo-potential calculations of Fritsch <i>et al.</i> [52] do not show degeneracy at this critical point
Valence band energy of spin–orbital splitting, E_{so} (eV)	0.019 at 300 K 0.036	[108]

Table 1.17 (Continued)

Wurtzite polytype AlN	Parameter	Comments/references
Valence band energy of crystal field splitting, E_{cr} (eV), Γ_7 on top of Γ_9	-0.225	[108]
Effective conduction band density of states (cm^{-3})	6.3×10^{18}	[78]
Effective valence band density of states (cm^{-3})	4.8×10^{20}	[78]
Index of refraction	n (3 eV) = 2.15 ± 0.05	
Dielectric constant (static)	9.14 at 300 K	By reflectivity [111]
	7.34	[78,112]
	8.5 ± 0.2 at 300 K	
	9.32 for $E//c$ (modeling)	[113]
	7.76 for $E \perp c$ (experiment)	[113]
Dielectric constant (high frequency)	4.6 at 300 K	[111]
	4.68	[78]
	4.77	
	4.84 at 300 K	Reflectivity
	4.35 for $E//c$ (modeling)	[113]
	4.16 for $E \perp c$ (experiment)	[113]
Infrared refractive index	2.1–2.2 at 300 K	Epitaxial films and monocrystal
	1.9–2.1 at 300 K	Polycrystalline films
	1.8–1.9 at 300 K	Amorphous films [87]
	3 for $E//c$ (modeling)	[113]
	2.8 for $E \perp c$ (experiment)	[113]
Effective electron mass, m_e	0.27 and $0.35m_0$	[14,114,115]
	$0.25\text{--}0.39m_0$	[107]
	$0.4m_0$ at 300 K	
	$m_e^// = 0.231 - 0.35m_0$	[52]
	$m_e^\perp = 0.242 - 0.25m_0$	
Effective hole masses (heavy)	$m_{hh}^// = 3.53m_0$ at 300 K	[116]
For k_z direction m_{hz} or $m_{hh}^//$	$2.02\text{--}3.13m_0$ at 300 K	[107]; from Mg binding energy
For k_x direction m_{hx} or m_{hh}^\perp	$m_{hh}^\perp = 10.42m_0$ at 300 K	[116]
	$m_{hh}^// = 1.869 - 4.41m_0$	[52]
	$m_{hh}^\perp = 2.18 - 11.14m_0$	[52]
Effective hole masses (light)	$3.53m_0, 0.24m_0$	At 300 K [116]
For k_z direction m_{lz} or $m_{lh}^//$	$m_{lh}^// = 1.869 - 4.41m_0$	[52]
For k_x direction m_{lx} or m_{lh}^\perp	$m_{lh}^\perp = 0.24 - 0.350m_0$	[52]
Effective hole masses (split-off band)	$0.25m_0$ at 300 K	[116]
	$3.81m_0$ at 300 K	
For k_z direction m_{soz} or $m_{ch}^//$	$m_{ch}^// = 0.209 - 0.27m_0$	[52]
For k_x direction m_{sox} or m_{ch}^\perp	$m_{ch}^\perp = 1.204 - 4.41m_0$	[52]

(Continued)

Table 1.17 (Continued)

Wurtzite polytype AlN	Parameter			Comments/references
Effective mass of density of state, m_v	7.26 m_0 at 300 K			[116]
Optical phonon energy (meV)	99.2			
$\nu_{\text{TO}}(E_1)$ phonon wave number (cm^{-1}) ^b	895	614	608	First column [117]; second column [118]; third column [113]
$\nu_{\text{LO}}(E_1)$ phonon wave number (cm^{-1})	671.6	821	888.9	See Table 1.30 for more details
$\nu_{\text{TO}}(A_1)$ phonon wave number (cm^{-1})	888	514	667.2	
$\nu_{\text{LO}}(A_1)$ phonon wave number (cm^{-1})	659.3	663	909	
$\nu(E_2)$ phonon wave number (cm^{-1})	303 ^a	426		
$n_{\text{TO}}(E_1)$ phonon wave number (cm^{-1})	657–673			[87,111,119,120]
$n_{\text{TO}}(A_1)$ phonon wave number (cm^{-1})	607–614 or 659–667			
$n_{\text{LO}}(E_1)$ phonon wave number (cm^{-1})	895–924			
$n_{\text{LO}}(A_1)$ phonon wave number (cm^{-1})	888–910			
$n^{(1)}(E_2)$ phonon wave number (cm^{-1})	241–252			
$n^{(2)}(E_2)$ phonon wave number (cm^{-1})	655–660			

The details of the energies of high symmetry points are given in Table 2.2. See Table 1.30 for additional details for phonon wave numbers. More details of effective masses can be found in Table 3.15. Temperature dependence of energy gap: $E_g = E_g(0) - 1.799 \times 10^{-3} T^2 / (T + 1462)$ (eV) by Guo and Yoshida [103].

^aRoom-temperature Raman, tentative.

^bFor more details regarding vibrational modes, refer to Section 1.3.1.

Phase transition from the wurtzite phase to the rock salt structure (space group O_h^5 ; lattice parameter 4.04 Å) takes place at the pressure of 17 GPa (~ 173 kbar) [109,110].

Parameters associated with the electrical and optical properties of zinc blende AlN are listed in Table 1.18. For details regarding the Luttinger parameters for the valence band in zinc blende AlN, refer to Table 2.16. Parameters associated with the mechanical properties of wurtzitic InN are tabulated in Table 1.19.

For wurtzite crystal structure, the surfaces of equal energy in Γ valley should be ellipsoids, but effective masses in the z -direction and perpendicular directions are estimated to be approximately the same.

Table 1.18 Parameters related to optical and electrical properties of zinc blende AlN.

Zinc blende polytype of AlN	Value	Comments/references
Bandgap energy (eV)	4.2; 6.0 5.8 All (theory)	All at 300 K [52]
Dielectric constant (static)	9.56	^a
Dielectric constant (high frequency)	4.46	[*]
Energy separation between Γ and X valleys E_{Γ} (eV)	~ 0.7	[52]
Energy separation between Γ and L valleys E_L (eV)	0.5	[84]
Spin-orbit splitting in valence band, Δ_{so} or E_{so} (eV)	~ 2.3	[52]
Deformation potential (eV)	3.9	[84]
Effective electron mass, m_e	0.019	[84]
Effective hole masses (heavy)	$m_{hh}^{[100]} = 1.02m_0$ $m_{hh}^{[111]} = 2.64m_0$ $m_{hh}^{[110]} = 1.89m_0$	[52]
Effective hole masses (light)	$m_{lh}^{[100]} = 0.37m_0$ $m_{lh}^{[111]} = 0.30m_0$ $m_{lh}^{[110]} = 0.32m_0$	[52]
Effective hole masses (split-off band), m_s , m_{ch} , or m_{so}	0.54 m_0	[52]
Luttinger parameter γ_1	1.85	[52]
Luttinger parameter γ_2	0.43	
Luttinger parameter γ_3	0.74	

^a C. Persson, and A. Ferreira da Silva, "Linear optical response of zinc-blende and wurtzite III-N (III = B, Al, Ga, and In)", Journal of Crystal Growth 305 pp. 408–413 (2007)

The parameters associated with thermal properties of wurtzitic InN are tabulated in Table 1.20.

The specific heat C_p of InN at constant pressure for $298\text{ K} < T < 1273\text{ K}$ [51] is $C_p = 38.1 + 1.21 \times 10^{-2}T$ ($\text{J mol}^{-1}\text{ K}^{-1}$). Refer to Table 1.31 for a detailed treatment of mechanical properties of InN.

The parameters associated with electrical and optical properties of wurtzitic InN are tabulated in Table 1.21.

Available parameters associated with the mechanical properties of zinc blende InN, primarily calculated, are tabulated in Table 1.22. Other parameters dealing with electrical and optical properties of zinc blende InN, primarily calculated, are listed in Table 1.23.

Table 1.19 Parameters related to mechanical properties of wurtzitic InN (in part after Ref. [36]).

Wurtzite InN	Value	Comments/references
Group of symmetry	C_{6v}^4 ($P6_3mc$)	
Molar volume ($\text{cm}^3 \text{mol}^{-1}$)	18.49	
Molar mass (g mol^{-1})	128.827	
Density (g cm^{-3})	6.89	
Lattice constants (\AA)	6.98	Measured by displacement
	6.81	X-ray, 298.15 K [122]
	$a = 3.548$	Epitaxial layers, X-ray [123];
	$a = 3.5446$	300 K [124]
	$a = 3.533$	
Bulk modulus B (GPa)	$c = 5.760$	Epitaxial layers, X-ray [123];
	$c = 5.7034$	300 K [124]
	$c = 5.693$	
dB/dP	165	
	140	[124]
	3.8	
Nanoindentation hardness (GPa)	11.2	[125]
Young's modulus (GPa)		Can be calculated using S parameters and Equation 2.10
Poisson's ratio, ν or σ_0		0.82, 0.68
Knoop's hardness (GPa)		
Deformation potential, E_{ds}	7.10 eV	Estimate
C_{11} (GPa)	223	[42]
C_{12} (GPa)	115	[42]
C_{13} (GPa)	92	$C_{31} = 70$ [42]
C_{33} (GPa)	224	205 [42]
C_{44} (GPa)	48	[42]

$E_g = E_g(0) + 3.3 \times 10^{-2} P$ (eV), where P is pressure in GPa [35,126]. For details of elastic constants and piezoelectric constants, see Table 2.19. $B_s = [C_{33}(C_{11} + C_{12}) - 2(C_{13})^2] / [C_{11} + C_{12} + 2C_{33} - 4C_{13}]$.

1.2 Gallium Nitride

Despite the fact that GaN has been studied far more extensively than the other group III nitrides, further investigations are still needed to approach the level of understanding of technologically important materials such as Si and GaAs. GaN growth often suffers from large background n-type carrier concentrations because of native defects and, possibly, impurities. The lack of commercially available native substrates

Table 1.20 Parameters related to thermal properties of wurtzitic InN (in part after Ref. [36]).

Wurtzite polytype InN	Value	Comments/references
Temperature coefficient	$dE_g/dT = -1.8 \times 10^{-4} \text{ eV K}^{-1}$	
Thermal expansion	$\Delta a/a = 2.70 \times 10^{-6} \text{ K}^{-1}$; $\Delta c/c = 3.40 \times 10^{-6} \text{ K}^{-1}$	At 190 K
	$\Delta a/a = 2.85 \times 10^{-6} \text{ K}^{-1}$; $\Delta c/c = 3.75 \times 10^{-6} \text{ K}^{-1}$	At 260 K
	$\Delta a/a = 3.15 \times 10^{-6} \text{ K}^{-1}$; $\Delta c/c = 4.20 \times 10^{-6} \text{ K}^{-1}$	At 360 K
	$\Delta a/a = 3.45 \times 10^{-6} \text{ K}^{-1}$; $\Delta c/c = 4.80 \times 10^{-6} \text{ K}^{-1}$	At 460 K
	$\Delta a/a = 3.70 \times 10^{-6} \text{ K}^{-1}$; $\Delta c/c = 5.70 \times 10^{-6} \text{ K}^{-1}$	At 560 K
	$\alpha_a = 3.8 \times 10^{-6} \text{ K}^{-1}$; $\alpha_c = 2.9 \times 10^{-6} \text{ K}^{-1}$	[124]
Thermal conductivity	$0.8 \pm 0.2 \text{ W cm}^{-1} \text{ K}^{-1}$ $0.45 \text{ W cm}^{-1} \text{ }^\circ\text{C}^{-1}$ $1.76 \text{ W cm}^{-1} \text{ }^\circ\text{C}^{-1}$, 300 K (estimate for ideal InN)	Estimate [127]
Heat of formation, $\Delta H_{298} \text{ (kcal mol}^{-1}\text{) (Wz)}$	-4.6	
Heat of atomization, $\Delta H_{298} \text{ (kcal mol}^{-1}\text{)}$	-175	
Melting point	1373 K 2146 K, vapor pressure 10^5 bar at 1100–1200 °C	[92]
Debye temperature	660 K at 300 K 370 K at 0 K	[124] [128]
Specific heat ($\text{J mol}^{-1} \text{ K}^{-1}$)	$C_p = 38.1 + 1.21 \times 10^{-2} T$	[51]
Heat capacity, $C_p \text{ (cal mol}^{-1} \text{ K}^{-1}\text{)}$	$9.1 + 2.9 \times 10^{-3} T$	298–1273 K
Entropy, $S^0 \text{ (cal mol}^{-1} \text{ K}^{-1}\text{)}$	10.4	298.15 K
TSFC ^w at formation, ΔH_f^0 (kcal mol ⁻¹)	-34.3, -30.5	Experimental 298.15 K
TSFC ^a at formation, ΔS_f^0 (kcal mol ⁻¹ K ⁻¹)	-25.3	Experimental 298.15 K
TSFC ^w at formation, $\Delta G_f^0 \text{ (kcal mol}^{-1}\text{)}$	-22.96	Experimental 298.15 K
TSFC ^w at fusion, $\Delta H_m \text{ (kcal mol}^{-1}\text{)}$	14.0	Theoretical
TSFC ^w at fusion, $\Delta S_m \text{ (cal mol}^{-1} \text{ K}^{-1}\text{)}$	$10.19 \text{ cal mol}^{-1} \text{ K}^{-1}$	Theoretical
N ₂ equilibrium vapor pressure	1 atm 10^5 atm	800 K 1100 K

^aTSFC: thermodynamic state function changes.

exacerbates the situation. These, together with the difficulties in obtaining p-type doping, and the arcane fabrication processes caused the early bottlenecks stymieing progress. Information available in the literature on many of the physical properties of GaN is in some cases still in the process of evolution, and naturally controversial. This

Table 1.21 Parameters related to electrical and optical properties of wurtzitic InN (in part after Ref. [36]).

Wurtzitic InN	Value	Comments/references
Bandgap energy, E_g (300 K)	1.89 eV, 1.5 eV, 0.78 eV	See Section 1.3.1 for an expanded discussion
Electron affinity		
Dielectric constant (static)	15.3	300 K [124]
Dielectric constant (static, ordinary direction)	$\epsilon_{0,ort} = 13.1$	300 K [128]
Dielectric constant (static, extraordinary direction)	$\epsilon_{0, } = 14.4$,	300 K [128]
Dielectric constant (high frequency)	8.4	300 K, using the Lyddane–Sachs–Teller relation
	9.3	($\epsilon_0/\epsilon_{high} = \omega_{LO}^2/\omega_{TO}^2$) [129,130] Heavily doped film, infrared reflectivity [131]
	5.8	[132]
Infrared refractive index	2.9	At 300 K [124]
	2.56	At 300 K and $\lambda = 1.0 \mu\text{m}$, interference method; $n = 3 \cdot 10^{20} \text{cm}^{-3}$ [131]
	2.93	At $\lambda = 0.82 \mu\text{m}$ [131]
	3.12	At $\lambda = 0.66 \mu\text{m}$ [131]
	Reported range: 2.80–3.05	
Energy separation between Γ and M–L valleys (eV)	2.9–3.9	300 K [124]
	~ 4.8	[52]
Energy separation between M–L valleys degeneracy	0.6	300 K [124]
	~ 0.7	[52]
Energy separation between Γ and A valleys (eV)	0.7–2.7	300 K [124]
	~ 4.5	[52]
Energy separation between A valley degeneracy	1	300 K [124]
	~ 0.6	[52]
Energy separation between Γ and Γ_1 valleys (eV)	1.1–2.6	300 K [124]
Energy separation between Γ_1 valley degeneracy (eV)	1	300 K [124]
Effective conduction band density of states	$9 \times 10^{17} \text{cm}^{-3}$	300 K [124]
Effective valence band density of states	$5.3 \times 10^{19} \text{cm}^{-3}$	300 K [124]
Valence band crystal field splitting, E_{cr}	0.017 eV	300 K [124]

Table 1.21 (Continued)

Wurtzitic InN	Value	Comments/references
Valence band spin-orbital splitting, E_{so}	0.003 eV	300 K [124]
Index of refraction	~2.9 at 300 K 2.56 at 300 K (interference method; $n = 3 \cdot 10^{20} \text{ cm}^{-3}$, $\lambda = 1.0 \mu\text{m}$) 2.93 3.12	[124] [131] [131] [131]
Effective electron mass, m_e^*	$0.11m_0$ $m_e^{\parallel} = 0.1 - 0.138m_0$ $m_e^{\perp} = 0.1 - 0.141m_0$	[133] [52] [52]
Effective hole masses (heavy), m_h	$1.63m_0$ at 300 K $0.5m_0$ at 300 K $m_{hh}^{\parallel} = 1.350 - 2.493m_0$ $m_{hh}^{\perp} = 1.410 - 2.661 m_0$	[32,134,135] [136] [52] [52]
Effective hole masses (light), m_{lp}	$0.27m_0$ at 300 K $m_{lh}^{\parallel} = 1.350 - 2.493m_0$ $m_{lh}^{\perp} = 0.11 - 0.196m_0$	[32,134,135] [52] [52]
Effective hole masses (split-off band), m_s	$0.65m_0$ at 300 K $m_{ch}^{\parallel} = 0.092 - 0.14m_0$ $m_{ch}^{\perp} = 0.202 - 3.422$	[32,134,135] [52] [52]
Effective mass of density of state, m_v	$1.65m_0$ at 300 K	[134,135]
Optical LO phonon energy (meV)	73 at 300 K	[124]

The details of the energies of high symmetry points are given in Table 2.3. More details of effective masses can be found in Table 2.19.

Table 1.22 Available parameters for mechanical for zinc blende InN.

Zinc blende InN	Value	Comments/references
Lattice constant	$a = 4.98 \text{ \AA}$	
Density (g cm^{-3})	6.97	Derived from X-ray data
Bulk modulus (GPa)	138–155, 145.6 [42]	$B_s = (C_{11} + 2C_{12})/3$
dB/dP		3.9–4.0
Young's modulus (GPa), Y_0 or E		$Y_0 = (C_{11} + 2C_{12}) \cdot (C_{11} - C_{12}) / (C_{11} + C_{12})$
Shear modulus (GPa)		$C' = (C_{11} - C_{12})/2$
Poisson's ratio, ν or σ_0		ν or $\sigma_0 = C_{12} / (C_{11} + C_{12})$
C_{11} (GPa)	187	See Ref. [42]
C_{12} (GPa)	125	See Table 1.31 for details
C_{44} (GPa)	86	

Table 1.23 Available electrical and optical properties of zinc blende InN, primarily calculated.

Zinc blende InN	Value	Comments/references
Bandgap energy, E_g (300 K)	2.2 eV	In the absence of any reliable data, the bandgap to a first extent can be assumed to be similar to that for Wz InN. See Ref. [137] for a detailed treatment
	1.5–2.1 (theory)	
	0.2 eV below the Wz polytype	[138]
Dielectric constant	8.4	LWL
	12.45	By $\frac{(2\epsilon_0^+ + \epsilon_0^{//})}{3}$ of wurtzitic form (the spur)
Dielectric constant (high frequency)		Using Lyddane–Sachs–Teller relation ($\epsilon_0/\epsilon_{\text{high}} = \omega_{\text{LO}}^2/\omega_{\text{TO}}^2$)
Refractive index at LWL	2.88 ± 0.30	Theory
at 600–800 nm	2.90 ± 0.30	—
at 900–1200 nm	2.90	Transmission interference
at 900–1200 nm	3.05 ± 0.30	Transmission interference
at 620 nm	2.65	NIRSR
Density (g cm^{-3})	6.97	Derived from X-ray data
Energy separation between Γ and X_1^+ valleys E_Γ (eV)	3	[52]
Energy separation between Γ and L valleys E_L (eV)	2.6	[52]
Spin–orbit splitting in valence band, Δ_{so} or E_{so} (eV)	0.006	[84]
Effective electron mass, m_e	$0.13m_0$	[52]
Effective hole masses (heavy)	$m_{\text{hh}}^{[110]} = 2.12 m_0$ $m_{\text{hh}}^{[100]} = 1.18 m_0$ $m_{\text{hh}}^{[111]} = 2.89 m_0$	[52]
Effective hole masses (light)	$m_{\text{lh}}^{[110]} = 0.20 m_0$ $m_{\text{lh}}^{[100]} = 0.21 m_0$ $m_{\text{lh}}^{[111]} = 0.19 m_0$	[52]
Effective hole masses (split-off band), m_s or m_{ch} or m_{so}	$0.36m_0$	[52]

LWL: long-wavelength limit; NIRSR: normal incidence reflectance of synchrotron radiation.

is in part a consequence of measurements being made on samples of widely varying quality. For this book, when possible we have disregarded the spurious determination. However, measurements are too few to yield a consensus, in which case the available data are simply reported.

The burgeoning interest in nitrides has led to substantial improvements in the crystal growth and processing technologies, thus overcoming many difficulties encountered earlier. Consequently, a number of laboratories consistently obtained high-quality GaN with room-temperature background electron concentrations as low as $5 \times 10^{16} \text{ cm}^{-3}$. The successful development of approaches leading to p-type GaN has led to the demonstration of excellent p–n junction LEDs in the UV, violet, blue, green, and even yellow bands of the visible spectrum with brightness suitable for outdoor displays, CW lasers, and UV detectors, including the ones for the solar blind region. Moreover, power modulation doped field effect transistors (MODFETs) also generically referred to as heterojunction field effect transistors (HFETs) have been developed. What follows reports on the state of knowledge regarding the physical properties of GaN.

1.2.1

Chemical Properties of GaN

Since Johnson *et al.* [139] first synthesized GaN in 1932, a large body of information has repeatedly indicated that GaN is an exceedingly stable compound exhibiting significant hardness. It is this chemical stability at elevated temperatures combined with its hardness that has made GaN an attractive material for protective coatings. Moreover, owing to its wide energy bandgap, it is also an excellent candidate for device operation at high temperatures and caustic environments. Although the hardness may have initiated the interest in GaN, it is the excellent semiconducting features that have piqued the attention of researchers. While the thermal stability of GaN allows freedom of high-temperature processing, the chemical stability of GaN presents a technological challenge. Conventional wet etching techniques used in semiconductor processing have not been as successful for GaN device fabrication. For example, Maruska and Tietjen [140] reported that GaN is insoluble in H_2O , acids, or bases at room temperature, but does dissolve in hot alkali solutions at very slow rates. Pankove [141] noted that GaN reacts with NaOH forming a GaOH layer on the surface and prohibiting wet etching of GaN. To circumvent this difficulty, he developed an electrolytic etching technique for GaN. Low-quality GaN has been etched at reasonably high rates in NaOH [142,143], H_2SO_4 [144], and H_3PO_4 [145–147]. Although these etches are extremely useful for identifying defects and estimating their densities in GaN films, they are not as useful for the fabrication of devices [148]. Well-established chemical etching processes do help for the device technology development, and the status of these processes in the case of GaN can be found in Volume 2, Chapter 1. Various dry etching processes reviewed by Mohammad *et al.* [149] and Pearton *et al.* [150] are promising possibilities and are discussed in Volume 2, Chapter 1.

1.2.2

Mechanical Properties of GaN

GaN has a *molecular weight* of $83.7267 \text{ g mol}^{-1}$ in the hexagonal wurtzite structure. The lattice constant of early samples of GaN showed a dependence on growth conditions, impurity concentration, and film stoichiometry [151]. These observations were

attributed to a high concentration of interstitial and bulk extended defects. A case in point is that the lattice constants of GaN grown with higher growth rates were found to be larger. When doped heavily with Zn [152] and Mg [153], a lattice expansion occurs because at high concentrations the group II element begins to occupy the lattice sites of the much smaller nitrogen atom. At room temperature, the lattice parameters of GaN platelets [18] prepared under high pressure at high temperatures with an electron concentration of $5 \times 10^{19} \text{ cm}^{-3}$ are $a = 3.1890 \pm 0.0003 \text{ \AA}$ and $c = 5.1864 \pm 0.0001 \text{ \AA}$. The freestanding GaN with electron concentration of about 10^{16} cm^{-3} , originally grown on sapphire (0001) by hydride vapor phase epitaxy (HVPE) followed by liftoff, has lattice constants of $a = 3.2056 \pm 0.0002 \text{ \AA}$ and $c = 5.1949 \pm 0.0002 \text{ \AA}$. For GaN powder, a and c values are in the range of 3.1893–3.190 and 5.1851–5.190 Å, respectively. Experimentally observed c/a ratio for GaN is 1.627, which compares well with 1.633 for the ideal case, and the u parameter calculated using Equation 1.1 is 0.367, which is very close to the ideal value of 0.375.

For more established semiconductors with the extended defect concentration from low to very low, such as Si, GaAs, and so on, the effect of doping and free electrons on the lattice parameter has been investigated rather thoroughly. In bulk GaN grown by the high-pressure technique, the lattice expansion by donors with their associated free electrons has been investigated [18]. However, large concentration of defects and strain, which could be inhomogeneous, rendered the studies of this kind less reliable in GaN layers. In spite of this, the effect of Mg doping on the lattice parameter in thin films of GaN has been investigated. Lattice parameters as large as 3.220–5.200 Å for a and c values, respectively, albeit not in all samples with similar hole concentrations, have been reported [154]. For GaN bulk crystals grown with high-pressure techniques and heavily doped (a small percentage) with Mg, the a and c lattice parameters were measured to be 3.2822–5.3602 Å [155]. Suggestions have been made that the c parameter of implanted GaN layers increases after implantation and languishes after annealing [156]. However, the a parameter could not be precisely measured because sharp off-normal diffraction peaks are needed to determine this parameter accurately.

For the zinc blende polytype, the calculated lattice constant, based on the measured Ga–N bond distance in Wz GaN, is $a = 4.503 \text{ \AA}$. The measured value for this polytype varies between 4.49 and 4.55 Å, while that in Ref. [18] is 4.511 Å, indicating that the calculated result lies within the acceptable limits [157]. A high-pressure phase transition from the Wz to the rock salt structure has been predicted and observed experimentally. The transition point is 50 GPa and the experimental lattice constant in the rock salt phase is $a_0 = 4.22 \text{ \AA}$. This is slightly different from the theoretical result of $a_0 = 4.098 \text{ \AA}$ obtained from first-principles nonlocal pseudopotential calculations [158].

Tables 1.6 and 1.10 compile some of the known properties of Wz GaN. Parameters associated with electrical and optical properties of Wz GaN are tabulated in Table 1.11. The same parameters associated with the zinc blende phase of GaN are tabulated in Table 1.12.

The bulk modulus of Wz GaN, which is the inverse of compressibility, is an important material parameter. Various forms of X-ray diffraction with the sample being under pressure can be used to determine the lattice parameters. Once the

lattice parameters are determined as a function of pressure, the pressure dependence of the unit cell volume can be obtained and fitted with an *equation of state* (EOS), such as the Murnaghan's EOS [159], and based on the assumption that the bulk modulus has a linear dependence on the pressure:

$$V = V_0 \left(1 + \frac{B'P}{B_0} \right)^{-1/B'} \quad (1.10)$$

where B_0 and V_0 represent the *bulk modulus* and the unit volume at ambient pressure, respectively, and B' the derivative of B_0 versus pressure. X-ray diffraction leads to the determination of the isothermal bulk modulus, whereas the Brillouin scattering leads to the adiabatic one. Nevertheless, in solids other than molecular solids, there is no measurable difference between the two thermodynamic quantities [160].

The bulk modulus (B) of Wz GaN has been calculated from first principles [161] and the first-principle orthogonalized *linear combination of atomic orbitals* (LCAO) method [158], leading to the values of 195 and 203 GPa, respectively. Another estimate for B is 190 GPa [158]. These figures compare well with the value of 194.6 GPa estimated from the elastic stiffness coefficient [79] and a measured value for 245 GPa [6].

The bulk modulus is related to the *elastic constants* through

$$B = \frac{(C_{11} + C_{12})C_{33} - 2C_{13}^2}{C_{11} + C_{12} + 2C_{33} - 4C_{13}} \quad (1.11)$$

and the range of bulk modulus values so determined is from about 173 to 245 GPa [160].

Using the room-temperature elastic constants of single-crystal GaN calculated by Polian *et al.* [38] yields an adiabatic bulk modulus, both *Voigt and Reuss* averages, of 210 GPa [91].

Earlier experimental investigations of the elastic constants of Wz GaN were carried out by Savastenko and Sheleg [162] using X-ray diffraction in powdered GaN crystals. The estimates of the *Poisson's ratio* from the early elastic coefficients ($\nu = C_{13}/C_{11} + C_{12}$) [162] and its measured [26] values of 0.372 (for $\nu\langle 0001 \rangle = (\Delta a/a_{\text{relax}})/(\Delta c/c_{\text{relax}})$) and 0.378 (for $\nu\langle 0001 \rangle = (\Delta a/a_0)/(\Delta c/c_0)$), respectively, are in good agreement (to avoid confusion the R value is defined as $R = -2C_{31}/C_{33}$). The experiments were performed on GaN layers on sapphire substrates because of X-ray diffraction. However, the results obtained later point to a Poisson's ratio of more near 0.2 as tabulated in Table 1.6 and depend on crystalline direction. The Poisson's ratio for the ZB case can be calculated from the elastic coefficients for that polytype as ν or $\sigma_0 = (C_{12}/C_{11} + C_{12})$ leading to values of about 0.352 as tabulated in Table 1.8. The Poisson's ratio varies along different crystalline directions as tabulated in Table 1.13 for AlN. It should be noted that there is still some spread in the reported values of elastic stiffness coefficients, as discussed in detail in the polarization sections of Section 2.12. More importantly, Kisielowski *et al.* [39] pointed out that expression

$$(\nu - 1)\langle 0001 \rangle = (\Delta a/a_{\text{relax}})/(\Delta c/c_{\text{relax}}), \quad (1.12)$$

where $\Delta a = a_{\text{meas}} - a_{\text{relax}}$ and $\Delta c = c_{\text{meas}} - c_{\text{relax}}$, should be used to calculate the Poisson's ratio, ν . Doing so leads to a Poisson's coefficient of $\nu_{\text{GaN}} = 0.2-0.3$.

Chetverikova *et al.* [163] measured the *Young's modulus* and Poisson's ratio of their GaN films. From the elastic stiffness coefficients, Young's modulus $E_{(0001)}$ is estimated to be 150 GPa [157,162]. Sherwin and Drummond [164] predicted the elastic properties of ZB GaN on grounds of values for those Wz GaN samples reported by Savastenko and Sheleg [162]. The elastic stiffness coefficients and the bulk modulus are compiled in Table 1.24. Considering the wide spread in the reported data more commonly used figures are also shown.

Wagner and Bechstedt [178] calculated the elastic coefficients of Wz GaN using a pseudopotential plane wave method and pointed out the discrepancies among the results from different calculations and measurements tabulated in Table 1.24. It is argued that reliable values produce $2C_{13}/C_{33} = 0.50-0.56$ and $\nu = 0.20-0.21$ [178]. The agreement between *ab initio* calculations [42,178] and some measure-

Table 1.24 Experimental and calculated elastic coefficients (C_{ij}), bulk modulus (B) and its pressure derivative (dB/dP), and Young's modulus (E or Y_0) and (in GPa) of Wz GaN and ZB GaN (in part from Ref. [160]).

Technique	C_{11}	C_{12}	C_{13}	C_{33}	C_{44}	B_0	B'	E
X-ray [162]	296	130	158	267	24.1	195		150
XAS						245	4	
EDX						188	3.2	
ADX						237	4.3	
Brillouin [38]	390	145	106	398	105	210		356
Brillouin	374	106	70	379	101	180		
Brillouin [166]	365	135	114	381	109	204		329
Brillouin [28]	373	141	80.4	387	94	192		362
Brillouin [169]	315	118	96	324	88	175		281
Brillouin [170]	373	141	80	387	94	192		362
Ultrasonic [171]	377	160	114	209	81.4	173		161
Ultrasonic [165]	370	145	110	390	90	208		343
Single crystal X-ray						207		
Most commonly used values	380	110			105			
PWPP [42]	367	135	103	405	95	202		363
FP-LMTO [165]	396	144	100	392	91	207		355
Kim [168]	431	109	64	476	126	201		461
PWPP (Wagner)	C_{11}	$515-C_{11}$	104	414		207		373
ZB GaN	253–264	153–165				60–68	200–237	3.9–4.3

The room-temperature elastic constants of single-crystal GaN have been determined by Polian *et al.* [38] yielding an adiabatic bulk modulus, both Voigt and Reuss, averages, of 210 GPa. The term $B' = dB/dP$ represents the derivative of B_0 versus pressure. EDX: energy dispersive X-ray; ADX: angular dispersive X-ray diffraction; XAS: X-ray absorption spectroscopy; PWPP: plane wave pseudopotential; FP-LMTO: full-potential linear muffin-tin orbital.

ments [38,165,166] is satisfactory. However, several calculations [167,168] and measurements [28,169–171] suffer from deviations in one or more of the values of elastic constants. The results from Savastenko and Sheleg [162] show excessive deviation for all the elastic constants and, therefore, should be avoided completely. The results from surface acoustic wave measurements of Deger *et al.* [165] on epitaxial epilayers have been corrected for piezoelectric stiffening and, therefore, are among the most reliable.

The vibrational properties of nitrides can best be described within the realm of mechanical properties. These vibrations actually serve to polarize the unit cell [172]. Phonons can be discussed under mechanical and optical properties. Here an arbitrary decision has been made to lump them with the mechanical properties of the crystal. Using GaN as the default, a succinct discussion of vibrational modes, some of which are active Raman modes, some are active in infrared (IR) measurements, and some are optically inactive called the silent modes, is provided [173]. Vibrational modes, which go to the heart of the mechanical properties, are very sensitive to crystalline defects, strain, and dopant in that the phonon mode frequencies and their frequency broadening can be used to glean very crucial information about the semiconductor. The method can also be applied to heterostructures and strained systems. Electronic Raman measurements can be performed to study processes such as electron–phonon interaction in the CW or time-resolved schemes. Time-resolved Raman measurements as applied to hot electron and phonon processes under high electric fields have important implication regarding carrier velocities. A case in point regarding GaN is treated in this context in Volume 3, Chapter 3.

The wurtzite crystal structure has the C_{6v}^4 symmetry and the group theory predicts the existence of the zone center optical modes A_1 , $2B_1$, E_1 , and $2E_2$. In a more simplified manner, one can consider that the stacking order of the Wz polytype is AaBb while that for the ZB variety is AaBbCc. In addition, the unit cell length of the cubic structure along $[1\ 1\ 1]$ is equal to the width of one unit bilayer, whereas that for the hexagonal structure along $[0\ 0\ 0\ 1]$ is twice that amount. Consequently, the phonon dispersion of the hexagonal structure along $[0\ 0\ 0\ 1]$ ($\Gamma \rightarrow A$ in the Brillouin zone) is approximated by folding the phonon dispersion for the ZB structure along the $[1\ 1\ 1]$ ($\Gamma \rightarrow L$) direction [174], as shown in Figure 1.12. Doing so reduces the TO phonon mode at the L point of the Brillouin zone in the zinc blende structure to the E_2 mode at the Γ point of the Brillouin zone in the hexagonal structure. This vibrational mode is denoted as E_2^H with superscript H depicting the higher frequency branch of the E_2 phonon mode. As indicated in the figure there is another E_2 mode at a lower frequency labeled as E_2^L . This has its genesis in zone folding of the transverse acoustic (TA) mode in the zinc blende structure. It should be noted that in the hexagonal structure there is anisotropy in the macroscopic electric field induced by polar phonons. As a result, both the TO and LO modes split into the axial (or A_1) and planar (or E_1) modes where atomic displacement occurs along the c -axis or perpendicular to the c -axis, respectively. This splitting is not shown in Figure 1.12 as it is very small, just a few meV, near zone center; phonon dispersion curves for GaN including the splitting of the A_1 and E_1 modes can be found in Volume 3, Figure 3.84.

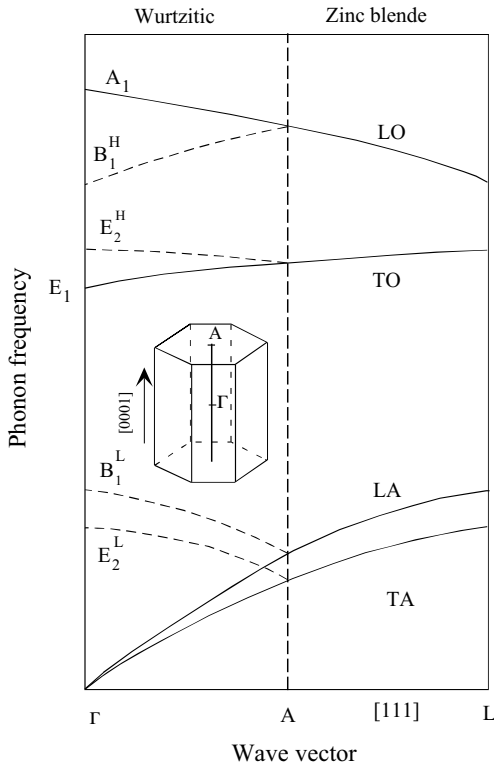


Figure 1.12 Schematic depiction of the phonon dispersion curves for ZB and Wz structures. Also shown are the Γ and A points of the zone in relation to the real space hexagonal structure. Phonon branches along the $[1\ 1\ 1]$ direction in the ZB structure are folded to approximate those of the wurtzite structure along the $[000\ 1]$ direction, because the unit cell length of the cubic structure along the $[1\ 1\ 1]$ direction is equal to the width of one unit bilayer, while that for the hexagonal structure along the $[000\ 1]$ directions is twice that amount. Patterned after Ref. [174].

As discussed below, in the context of hexagonal structures, group theory predicts eight sets of phonon normal modes at the Γ point, namely $2A_1 + 2E_1 + 2B_1 + 2E_2$. Among them, one set of A_1 and E_1 modes are acoustic, while the remaining six modes, namely $A_1 + E_1 + 2B_1 + 2E_2$, are optical modes. As shown in Figure 1.12, one A_1 and one B_1 mode (B_1^H) derive from a singly degenerate LO phonon branch of the zinc blende system by zone folding, whereas one E_1 and one E_2 mode (E_2^H) derive from a doubly degenerate TO mode in the cubic system.

The first-order phonon Raman scattering is due to phonons near the Γ point zone center, that is, with wave vector $k \approx 0$, because of the momentum conservation rule in the light scattering process. Raman measurements typically are employed to probe the vibrational properties of semiconductors. When performed along the direction perpendicular to the c -axis or the $(000\ 1)$ plane, the nomenclature used to describe this configuration is depicted as $Z(XY, XY)\bar{Z}$. Here, following Porto's notation [175] $A(B, C)D$ is used to describe the Raman geometry and polarization, where A and D

represent the wave vector direction of the incoming and scattered light, respectively, whereas B and C represent the polarization of the incoming and scattered light. In Raman scattering, all the above-mentioned modes, with the exception of B_1 modes, are optically active. Because of their polar nature, the A_1 and E_1 modes split into longitudinal optical (A_1 -LO and E_1 -LO) meaning beating along the c -axis, and transverse optical (A_1 -TO and E_1 -TO), meaning beating along the basal plane. To reiterate, the A_1 and B_1 modes give atomic displacements along the c -axis, while the others, E_1 and E_2 , give atomic displacements perpendicular to the c -axis, meaning on the basal plane. Here, the A_1 and E_1 modes are both Raman and IR active whereas the two E_2 modes are only Raman active and the two B_1 modes are neither Raman nor IR active, meaning silent modes. In the $Z(XY, XY)\bar{Z}$ configuration, only the E_2^L (or E_2^L or E_2 low), E_2^H (or E_2^H or E_2 high), and A_1 (LO) modes should be observable. In particular, in $Z(X, X)\bar{Z}$ and $Z(Y, Y)\bar{Z}$ geometries, all three modes are observable, while in $Z(X, Y)\bar{Z}$ or $Z(Y, X)\bar{Z}$ geometries only E_2 modes are detected [175]. The details of the mode–Raman configuration relationship are tabulated in Table 1.25. Shown in Figure 1.13 are the modes in the Raman backscattered geometries in relation to hexagonal crystalline orientation that can be used to sense the various phonon modes indicated.

The acoustic modes, which are simple translational modes, and the optical modes for wurtzite symmetry are shown in Figure 1.14. The calculated phonon dispersion curves [57] for GaN are shown in Figure 1.15. There is another way to describe the number of vibrational modes in zinc blende and wurtzitic structures, which is again based on symmetry arguments. In the wurtzite case [66], the number of atoms per unit cell $s = 4$, and there are total of 12 modes, the details of which are tabulated in Table 1.26. This table also holds for the zinc blende polytypes with $s = 2$. This implies a total of six modes in zinc blende as opposed to 12 in wurtzite, three of which are acoustical (1 LA and 2 TA) and the other three are optical (1 LO and 2 TO) branches. These phonon modes for a wurtzite symmetry, specifically the values for wurtzite GaN, are listed in Table 1.27 obtained from Refs [56,157,176,177] along with those obtained from first-principles pseudopotential calculations [161,178]. Also listed are TO and LO optical phonon wave numbers of ZB GaN [25,179].

Table 1.25 Raman measurement configuration needed to observe the phonon modes in hexagonal nitrides.

Mode	Configuration
A_1 (TO), E_2	$X(Y, Y)\bar{X}$
A_1 (TO)	$X(Z, Z)\bar{X}$
E_1 (TO)	$X(Z, Y)\bar{X}$
E_1 (TO), E_1 (LO)	$X(Y, Z)Y$
E_2	$X(Y, Y)Z$
E_2	$Z(Y, X)\bar{Z}$
A_1 (LO), E_2	$Z(Y, Y)\bar{Z}$

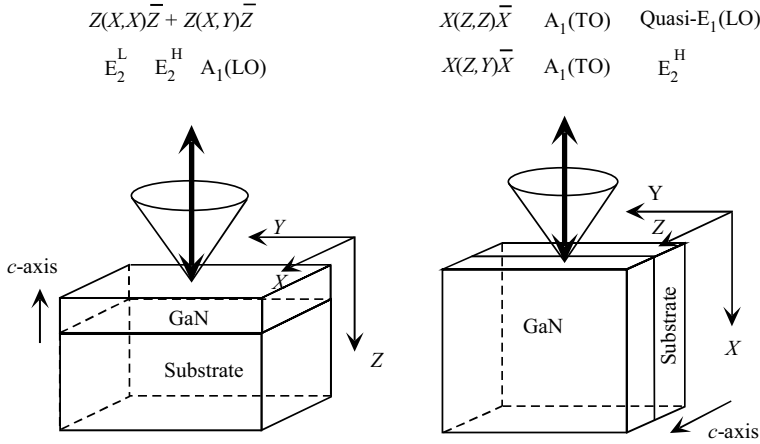


Figure 1.13 Schematic representation of two Raman configurations with incident and scattered light directions in the backscattering geometry for $Z(X, X)\bar{Z} + Z(X, Y)\bar{Z}$ configuration to sense E_2^L , E_2^H , and $A_1(\text{LO})$ modes, $X(Z, Z)\bar{X}$ configuration to sense $A_1(\text{TO})$ and quasi- $E_1(\text{LO})$ modes, and $X(Z, Y)\bar{X}$ configuration to sense $A_1(\text{TO})$ and E_2^H modes.

Owing to the presence of elastic strain, thin epilayers have different phonon energies compared to the bulk samples. In the general case, strain can give rise to a shift and splitting of phonon modes. However, for uniaxial strain along the c -axis or biaxial strain in the c -plane, the crystal retains its hexagonal symmetry resulting in only a shift of the phonon frequencies. The strain effects on GaN optical phonon energies have been studied experimentally [181] and theoretically [178]. Within a perturbative approach, the change in the frequency of a given phonon λ under symmetry-conserving stress can be expressed in terms of the two strain components, ε_{xx} and ε_{zz} , representing perpendicular and parallel to the z -axis, respectively, as $\Delta\Omega_\lambda = 2 a_\lambda \varepsilon_{xx} + b_\lambda \varepsilon_{zz}$, where a_λ and b_λ are the corresponding deformation potential constants. The derivation of strain values from the Raman measurements of phonon frequencies is straightforward, once the phonon deformation potentials are known. Davydov *et al.* [181] combined high-resolution X-ray diffraction (HRXRD) measurements and Raman spectroscopy results to determine the phonon deformation potentials in GaN epitaxial layers grown on 6H-SiC. The strain components were obtained by comparing the lattice constants of the epitaxial layers with those of the strain-free GaN ($a_0 = 3.1880 \text{ \AA}$, $c_0 = 5.18561 \text{ \AA}$). The Raman spectrum of a strain-free $300 \mu\text{m}$ thick GaN layer grown on sapphire was used as a reference. Also, using their relation to the hydrostatic pressure coefficients [6] through the bulk elastic coefficients, the sets of phonon deformation potentials were derived for most of zone center optical phonons. As seen in Table 1.27, except for the A_1 -TO mode, the phonon energies and the deformation potentials reported by Davydov *et al.* [181] agree well with the pseudopotential plane wave calculations reported by Wagner and Bechstedt [178]. Wagner and Bechstedt argue that the published conversion factors

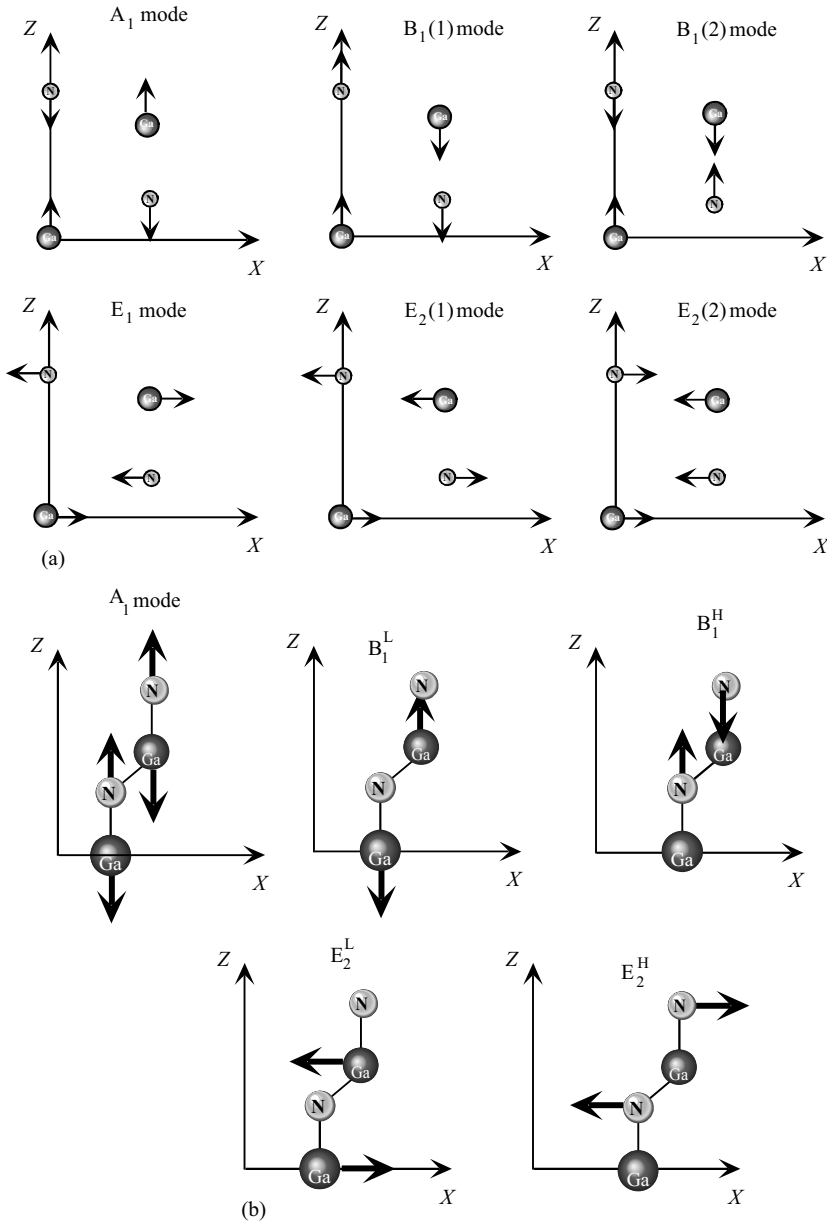


Figure 1.14 Atomic vibrations in Wz GaN. The larger atom represents Ga while the smaller one is for N. $X=(100)$, $Y=(010)$, and $Z=(001)$ represent the optical polarization directions: (a) for general wave vector and (b) for zone center phonons.

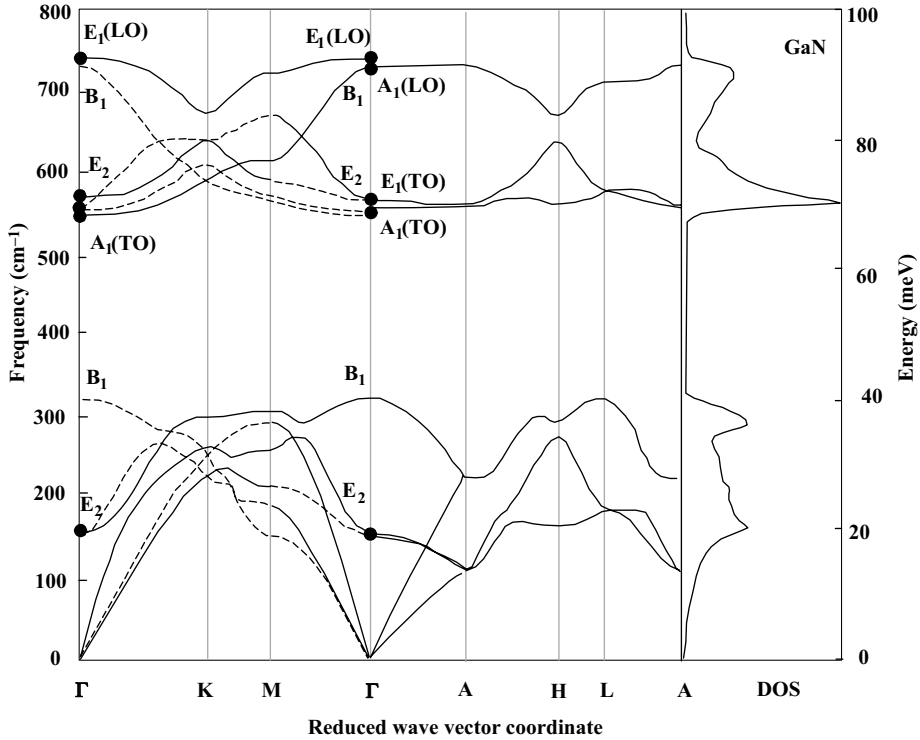


Figure 1.15 Calculated phonon dispersion curves and phonon density of states for hexagonal bulk GaN. The solid and dashed lines correspond to the Λ_1 (or T_1) and Λ_2 (or T_2) irreducible representations (following Ref. [180]), respectively. Note how close the $E_1(\text{LO})$ and $A_1(\text{LO})$ modes are, making high-quality samples with sharp modes imperative for their experimental delineation [169].

Table 1.26 Acoustic and optical phonon modes in a crystal with wurtzite symmetry such as GaN, AlN, and InN, where s represents the number of atoms in the basis.

Mode type	Number of modes
LA	1
TA	2
Total acoustic modes	3
LO	$s - 1$
TO	$2s - 2$
All optical modes	$3s - 3$
All modes	$3s$

The s parameter for wurtzite symmetry is 4. This table is also applicable to the zinc blende case but with $s = 2$.

Table 1.27 (a) Zone center optical phonon wave numbers (in units of cm^{-1}) of GaN obtained from Raman scattering at 300 K compiled by Akasaki and Amano [157] (Wz) and Huang *et al.* [177] (Wz template). Also shown are the calculated values. (b) Measured phonon wave numbers (in units of cm^{-1}) for wurtzitic GaN. (c) Zinc blende phase phonon wave numbers for zinc blende GaN [179] (theory [59]).

Phonon mode	Wz [157,177]	Wz template [177]	Wz relaxed		Wz unstrained (calculated) [178]		Deformation potentials – Wz			
			[169]	[178]	a_λ	b_λ	Raman [181]		Calculated [178]	
							a_λ	b_λ	a_λ	b_λ
E_1 -TO	556–559	558.5	558.8	568	-820 ± 25	-680 ± 50	-717	-591		
A_1 -TO	533–534	532.5	531.8	540	-630 ± 40	-1290 ± 80	-640	-695		
E_1 -LO	741–741	745.0	741	757			-775	-703		
A_1 -LO	710–735	737.0	734	748			-664	-695		
E_2^L	143–146		144	142	115 ± 25	-80 ± 35	75	4		
E_2^H	560–579		567.6	576	-850 ± 25	-920 ± 60	-742	-715		
B_1^L				337			-334	-275		
B_1^H				713			-661	-941		

Table 1.27 (Continued)

(b)	
Phonon mode	Wz unstrained (measured) (collected in Refs [174,178], but based on Refs [6,169])
E_1 -TO	558.8
A_1 -TO	531.8
E_1 -LO	741
A_1 -LO	741
E_2^L	144
E_2^H	567.6
B_1^L	
B_1^H	

(c)	
Mode	Mode
$LO(\Gamma)$ (cm^{-1})	$LO(L)$ (cm^{-1})
$TO(\Gamma)$ (cm^{-1})	$TO(L)$ (cm^{-1})
$LO(X)$ (cm^{-1})	$LA(L)$ (cm^{-1})
$TO(X)$ (cm^{-1})	$TA(L)$ (cm^{-1})
$LA(X)$ (cm^{-1})	TO (cm^{-1})
$TA(X)$ (cm^{-1})	LO (cm^{-1})

GaN on sapphire, about 50–70 μm thick, at 300 K.

between the luminescence or Raman shifts and the corresponding biaxial stress are seldom directly measured data. They are either obtained using elastic constants or are constructed from deformation potentials, which have been obtained by means of additional hydrostatic pressure coefficients. Owing to these varying procedures and different sets of parameters used to extract the conversion coefficients from the raw experimental data, discrepancies in the experimental reports of deformation potentials are present.

1.2.3

Thermal Properties of GaN

The lattice parameter of semiconductors depends on temperature and is quantified by *thermal expansion coefficient* (TEC), which is defined as $\Delta a/a$ or α_a and $\Delta c/c$ or α_c , for in-plane and out-of-plane configurations, respectively. It depends on stoichiometry, extended defects, and free-carrier concentration. As in the case of the lattice parameter, a scatter exists in TEC particularly for nitrides as they are grown on foreign substrates with different thermal and mechanical properties. Measurements made over the temperature range of 300–900 K indicate the mean coefficient of thermal expansion of GaN in the *c*-plane to be $\Delta a/a = \alpha_a = 5.59 \times 10^{-6} \text{ K}^{-1}$. Similarly, measurements over the temperature ranges of 300–700 and 700–900 K, respectively, indicate the mean coefficient of thermal expansion in the *c*-direction to be $\Delta c/c = \alpha_c = 3.17 \times 10^{-6}$ and $7.75 \times 10^{-6} \text{ K}^{-1}$, respectively [140]. Sheleg and Savastenko [49] reported a TEC near 600 K for perpendicular and parallel to the *c*-axis of $4.52 \pm 0.5 \times 10^{-6}$ and $5.25 \pm 0.05 \times 10^{-6} \text{ K}^{-1}$, respectively. Leszczynski and Walker [182] reported α_a values of 3.1 and $6.2 \times 10^{-6} \text{ K}^{-1}$ for the temperature ranges of 300–350 and 700–750 K, respectively. The α_c values in the same temperature ranges, in order, were 2.8 and $6.1 \times 10^{-6} \text{ K}^{-1}$.

In a similar vein, GaN and other allied group III nitride semiconductors are grown at high temperatures and also subjected to increased junction temperatures during operation of devices such as amplifiers and light emitting devices. As such, the structures are subjected to thermal variations as well. In this context, it is imperative to have knowledge of the thermal expansion coefficients, which are termed as TEC. Assuming that these figure remain the same with temperature, the linear expansion coefficients for the *a* and *c* parameters are tabulated in Tables 1.10 and 1.28 for heteroepitaxial GaN. However, it is instructive to know the temperature dependence of these parameters, which is shown in Figure 1.16.

Being grown on various substrates with different thermal expansion coefficients leads to different dependencies of the lattice parameter on temperature. Temperature dependence of GaN lattice parameter has been measured for a bulk crystal (grown at high pressure) with a high free-electron concentration ($5 \times 10^{19} \text{ cm}^{-3}$), a slightly strained homoepitaxial layer with a low free-electron concentration (about 10^{17} cm^{-3}), and a heteroepitaxial layer (also with a small electron concentration) on sapphire [88]. The results of such study are tabulated in Table 1.28.

It can be seen that the bulk sample with a high free-electron concentration exhibits a thermal expansion that is about 3% higher as compared to the homoepitaxial layer.

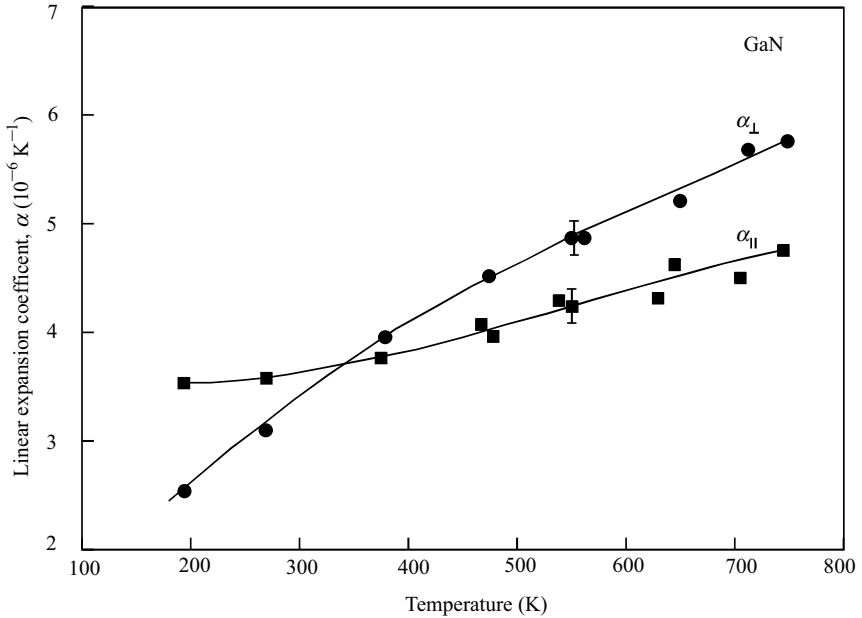


Figure 1.16 Wz GaN coefficient of linear thermal expansion versus temperature for basal plane (α_{\parallel}), a parameter, and out of the basal plane (α_{\perp}), c parameter, directions [49].

As for the case of the heteroepitaxial layer on sapphire, the thermal expansion of the substrate affects the dependence of the lattice parameter on temperature.

Various spectroscopic techniques, such as Auger electron spectroscopy, X-ray photoemission spectroscopy (XPS), and electron energy loss spectroscopy (EELS) have been very useful for the study of surface chemistry of GaN. Building on earlier investigations of the thermal stability of GaN by Johnson *et al.* [139] and employing

Table 1.28 Lattice parameters for GaN samples at various temperatures (lattice parameters c were measured with accuracy of 0.0002 Å, lattice parameter a with accuracy of 0.0005 Å) [88].

T (K)	GaN bulk, $n = 5 \times 10^{19} \text{ cm}^{-3}$		Homoepitaxial GaN on conductive GaN substrate		GaN on sapphire	
	c (Å)	a (Å)	c (Å)	a (Å)	c (Å)	a (Å)
20	5.1836	3.1867	5.1822	3.1867		
77	5.1838	3.1868	5.1824	3.1868	5.1846	3.1842
295	5.1860	3.1881	5.1844	3.1881	5.1865	3.1859
500	5.1885	3.1903	5.1870	3.1903	5.1888	3.1886
770	5.1962	3.1945	5.1944	3.1945	5.1952	3.1941

the aforementioned techniques, the thermal stability and dissociation of GaN have been examined further. As indicated earlier, the materials characteristics depend, to a large extent, on defects and impurities, which in turn depend somewhat on growth conditions. Because of this the materials, obtained from various sources, studied in various laboratories exhibit different characteristics. This led to inconsistent results from different laboratories. While some experimental studies on GaN stability conducted at high temperatures suggested that significant weight losses occur at temperatures as low as 750 °C, others contradicted this proposition and suggested that no significant weight loss should occur even at a temperature of 1000 °C. Sime and Margrave [183] followed the investigation by Johnson *et al.* [139] by studying the evaporation of GaN and Ga metal in the temperature range 900–1150 °C under atmospheric pressure in N₂, NH₃, and H₂ environments with an emphasis on the formation and decomposition equilibrium.

The *heat of evaporation* was determined and the existence of (GaN)_x polymers in the gas phase was suggested. Morimoto [184] and Furtado and Jacob [185] observed that GaN is less stable in an HCl or H₂ atmosphere than in N₂. Some controversy exists regarding the process steps that dictate the decomposition of GaN. Using mass spectroscopy, Gordienko *et al.* [186] noted that (GaN)₂ dimers are the primary components of decomposition. Others [187,188] found only N₂⁺ and Ga⁺ to be the primary components in the vapor over GaN. On the basis of measurements of the apparent vapor pressure, Munir and Searcy [189] calculated the *heat of sublimation* of GaN to be 72.4 ± 0.5 kcal mol⁻¹. Thurmond and Logan [190] determined the equilibrium N₂ pressure of GaN as a function of temperature by measuring the partial pressure ratios existing in a (H₂CNH₃) gas mixture streaming over Ga and GaN. Thermal stability of GaN was taken up later by Karpinski *et al.* [191] with a detailed investigation of the problem at high temperatures and under pressure up to 60 kbar by employing a tungsten carbide anvil cell activated by a gas pressure technique.

The bond strength in gallium nitride is high with bonding energy of 9.12 eV/molecule [192], particularly as compared to the more conventional semiconductors such as GaAs, which has a bonding energy of 6.5 eV/atom pair. As a result, the free energy of GaN is very low in relation to the reference states of the free N and Ga atoms. However, the N₂ molecule is also strongly bonded with 4.9 eV/atom. Therefore, the free energies of the constituents of GaN (Ga and N₂) at their normal states are close to that of the GaN crystal as illustrated in Figure 1.17, where the free energy of GaN (1 mol) and the free energy of the sum of its constituents (Ga + 1/2N₂) are shown as a function of temperature and N₂ pressure. As the temperature increases, the Gibbs free energy, $G(T)$, of the constituents decreases faster than $G(T)$ of the GaN crystal. More importantly, GaN becomes thermodynamically unstable at high temperatures. The crossing of $G(T)$ curves determines the equilibrium temperature where GaN coexists with its constituents at a given N₂ pressure. The application of pressure increases the free energy of the constituents more than $G(T)$ of the GaN crystal, which causes the equilibrium point to shift to higher temperatures, increasing the range of GaN stability.

The data on phase diagrams of GaN are limited and contradictory by reason of high melting temperatures (T_m) and high nitrogen dissociation pressures ($P_{N_2}^{dis}$). Dissociation

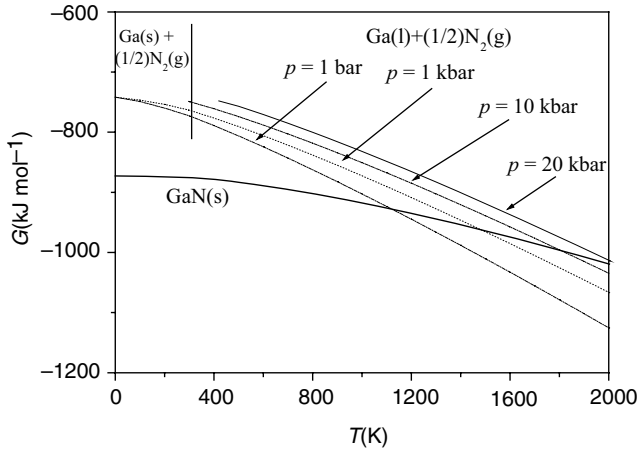


Figure 1.17 Gibbs free energy of GaN and its constituents as a function of temperature and pressure [192].

pressure of MN, where M stands for Al, Ga, and In, and N for nitrogen, is defined as the nitrogen pressure at the thermal equilibrium of the reaction [193]: $MN(s) = M(l) + 1/2N_2(g)$, where s, l, and g stand for solid, liquid, and gas states, respectively. Reported values for $P_{N_2}^{dis}$ for GaN [193] show large discrepancies [191,194]. Specifically, in the high-pressure range, the partial pressure, p , versus the inverse temperature, $1/T$, curve of Karpinski *et al.* deviates markedly from the linear dependence proposed by Thurmond and Logan as shown in Figure 1.18. Despite the discrepancies, there is a good agreement in the Gibbs free energy with $\Delta G^0 = 32.43T - 3.77 \times 10^4 \pm 700 \text{ cal mol}^{-1}$ for GaN synthesis between the two references. The value of enthalpy ΔH^0 ($-37.7 \text{ kcal mol}^{-1}$) is in good agreement as well with that estimated by Madar *et al.* [194].

The stars in Figure 1.18 indicate the melting point of AlN at $T_{AlN}^M = 3487 \text{ K}$, GaN at $T_{GaN}^M = 2791 \text{ K}$, and InN at $T_{InN}^M = 2146 \text{ K}$. The GaN and InN melting points so indicated may underestimate the real values, as perhaps a sufficient overpressure was not maintained. Line fits correspond to $8.3 \times 10^9 \exp(-5.41 \text{ eV}/kT)$, $1.5 \times 10^{14} \exp(-3.28 \text{ eV}/kT)$, and $7.9 \times 10^{17} \exp(-2.78 \text{ eV}/kT)$ bar for AlN, GaN, and InN, respectively. The data over the larger temperature range are those compiled by Ambacher [196]. The results of Madar *et al.* [194], Thurmond and Logan [190], and Karpinski *et al.* [191] are also shown in a limited temperature range. For GaN (see Figure 1.18), the nitrogen dissociation pressure equals 1 atm at approximately 850 °C and 10 atm at 930 °C. At 1250 °C, GaN decomposed even under pressure of 10 000 bar of N_2 . The turning over of the partial pressure for GaN and InN at temperatures approaching the melting point may need to be reexamined. What is clear, however, is that GaN and particularly InN have very high partial pressures that make it imperative to maintain high fluxes of N during growth. It should, therefore, come as no surprise that the incorporation of nitrogen is not a trivial problem at high temperatures. For the pressures below equilibrium at a given temperature, the thermal dissociation occurs at a slow and apparently constant rate suggesting a diffusion-controlled

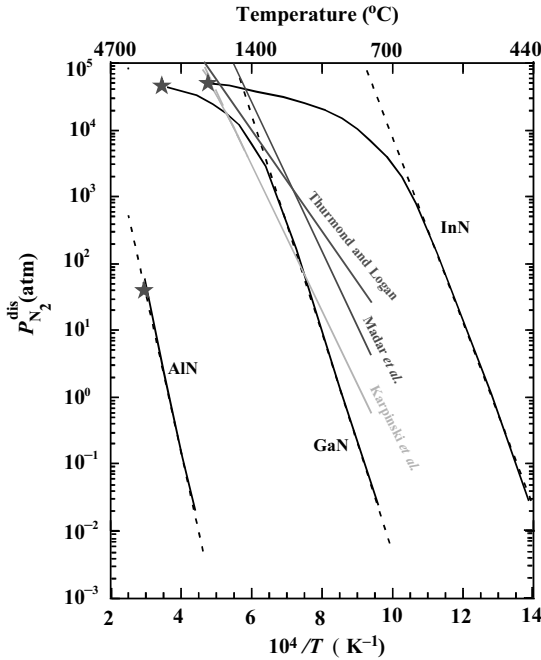


Figure 1.18 Equilibrium N_2 pressure over the $MN(s) + M(l)$ systems corresponding to GaN (336 kJ mol^{-1}), 3.9 eV (379 kJ mol^{-1}), and 4.3 eV (414 kJ mol^{-1}) for InN, GaN, and AlN, respectively. Caution should be exercised as there is significant deviation from the activation line for GaN and InN. This may simply be a matter of not being able to maintain sufficient pressure on GaN and InN at very high temperatures to reach the real melting point. The melting points of the three binaries are indicated by stars. The desorption activation energies, E_{MN} , determined by straight line fits to the data points are 3.5 eV

process of dissociation. Expanded equilibrium vapor pressure data inclusive of GaAs and InP in addition to the three nitride binaries reported by Matsuoka [197] are shown in Figure 1.19. Melting points and other thermodynamic characteristics of III-N compounds are given in Tables 1.10, 1.16, and 1.20 as compiled by Popovici and Morkoç [198] as well as those collected from various sources as indicated in the pertinent tables.

Investigations utilizing epitaxial thin films of GaN, as well as AlN and InN, have been conducted by Ambacher *et al.* [199], who heated the samples in vacuum and recorded the partial pressure of relevant gases with a quadrupole mass spectrometer. Desorption spectra were then analyzed [200] to find the binding energies of various desorbed species as well as the thermal stability of the sample for a given thermal treatment. As expected, the nitrogen partial pressure increases exponentially above $T_E = 850^\circ\text{C}$ for GaN underscoring the point that the decomposition temperature in vacuum is much lower than the melting point shown in Figure 1.18. The rate of

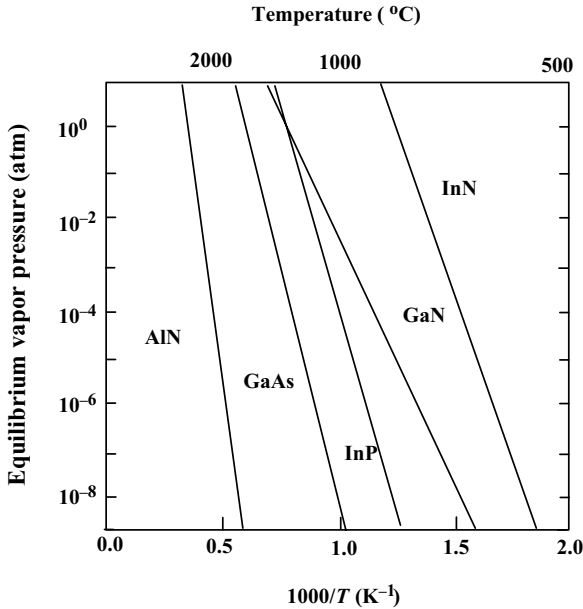


Figure 1.19 Equilibrium vapor pressure of N_2 over AlN, GaN and InN, the sum of As_2 and As_4 over GaAs, and the sum of P_2 and P_4 over InP [197].

nitrogen evolution $\Phi(N)$ was set equal to the rate of decomposition, and the slope of $\ln[\Phi(N)]$ versus $1/T$ gives the effective activation energy of the decomposition in vacuum as compared to those shown in Figure 1.18. The decomposition rate equals the desorption of one monolayer every second ($\Phi_N = 1.5 \times 10^{15} \text{ cm}^{-2} \text{ s}^{-1}$) at 970°C , and the activation energy of the thermally induced decomposition is determined to be $E_{MN} = 3.9 \text{ eV}$ (379 kJ mol^{-1}) for GaN.

Despite some disagreement, as mentioned above, investigations of the equilibrium nitrogen overpressure versus temperature, $P_{N_2}-T$, for GaN [92,190,201], including a very complete and consistent set of data obtained by Karpinski *et al.* [191,202] have set the stage for bulk template growth as well as setting benchmarks for growth of GaN by nonequilibrium methods. Those authors employed direct synthesis and decomposition experiments and used the gas pressure technique (for pressures up to 20 kbar) and the high-pressure anvil method beyond the reach of gas pressure technique (up to 70 kbar). The results of these experiments are shown in Figure 1.20 [203,204]. The message in the form of N_2 partial pressure is that one must stay below the decomposition curve. This means that the selection of GaN synthesis temperature directly depends on the pressure that the vessel can provide. For example, if a pressure of 20 kbar is all that is available, then the temperature should be kept below about 1660°C . For a review of the stability of GaN as well as the growth GaN templates, the reader is referred to Ref. [192].

As alluded to earlier, nitride semiconductors in general and GaN in particular are considered for high-power/high-temperature electronic and optoelectronic devices

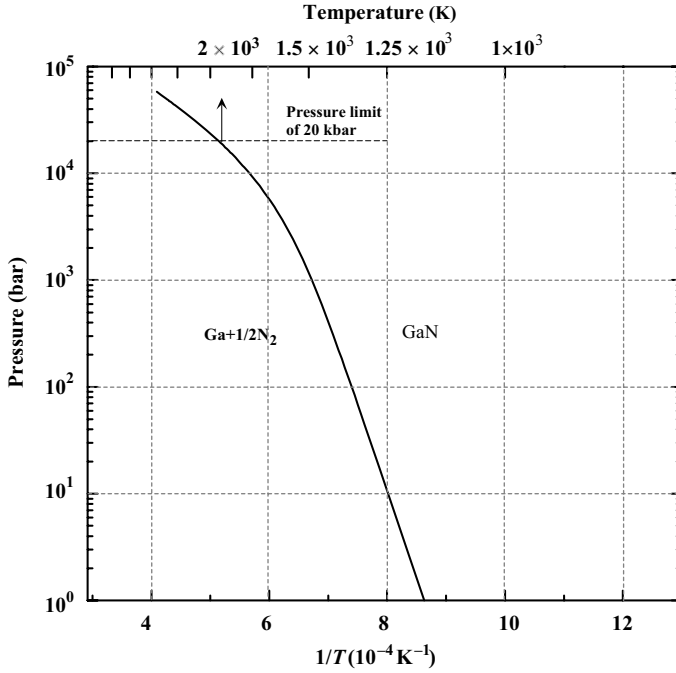


Figure 1.20 N_2 partial pressure as a function of temperature GaN. Ref. [192], originally in Refs [203,204].

where thermal dissipation is a key issue. Device applications assure that the *thermal conductivity* (κ) is an extremely important material property. Thermal conductivity is a kinetic property determined by contributions from the vibrational, rotational, and electronic degrees of freedom, and as such it is related to the mechanical properties of the material. However, for convenience, this property is generally categorized under the thermal properties of nitrides in this book. The electronic thermal conductivity contribution is negligible for carrier concentrations $\leq 10^{19} \text{ cm}^{-3}$. The heat transport is predominantly determined by phonon–phonon Umklapp scattering, and phonon scattering by point and extended defects such as vacancies (inclusive of the lattice distortions caused by them), impurities, and isotope fluctuations (mass fluctuation) as elaborated on by Slack *et al.* [91]. For pure crystals, phonon–phonon scattering, which is ideally proportional to T^{-1} above the Debye temperature, is the limiting process.

The lattice contribution (phonon scattering) to the thermal conductivity, κ , in a pure solid is obtained from the kinetic theory as [205]

$$\kappa_{\text{lattice}}(T) = \frac{1}{3} v_s C_{\text{lattice}}(T) L(T), \quad (1.13)$$

where T is the temperature, v_s is the velocity of sound (nearly independent of temperature), $C_{\text{lattice}}(T)$ is the lattice specific heat, and $L(T)$ is the phonon mean free length. In nearly all materials, the thermal conductivity, $\kappa(T)$, first increases with temperature, reaches a maximum (κ_{max}) at some characteristic temperature T_{ch} , and

then decreases. At low temperatures, L is relatively long and is dominated by extrinsic effects such as “defects” and/or finite crystal size and $C_{\text{lattice}}(T) \sim (T/\theta_D)^3$, where θ_D is the Debye temperature. As the temperature increases, $C_{\text{lattice}}(T)$ begins to saturate and the intrinsic temperature-dependent Umklapp processes become dominant, leading to a decrease in L .

The other contribution, the electronic contribution, to the thermal conductivity is negligible for carrier concentrations $\leq 10^{19} \text{ cm}^{-3}$. It can be expressed as [206]

$$\kappa_{\text{electr}}(T) = \frac{\pi^2 n k_B^2 T \tau_{\text{electr}}}{3 m_c^*}, \quad (1.14)$$

where n is the carrier density, k_B is the Boltzmann constant, τ_{electr} is the scattering time of the electrons, and m_c^* is the conduction band effective mass.

The first measurements of κ of GaN were by Sichel and Pankove [207] on “bulk” GaN (400 μm of material grown by HVPE) as a function of temperature (25–360 K): $\kappa \cong 1.3 \text{ W cm}^{-1} \text{ K}^{-1}$ (along the c -axis) at 300 K. This room-temperature value measured is a little smaller than the value of $1.7 \text{ W cm}^{-1} \text{ K}^{-1}$ predicted in 1973 [77] and much smaller than the $\kappa \sim 4.10 \text{ W cm}^{-1} \text{ K}^{-1}$ calculated by Witek [208]. Using the elastic constants reported by Polian *et al.* [38], Slack *et al.* [91] calculated a Debye temperature of 650 K, which led to a more recent thermal conductivity at 300 K for GaN of $\kappa = 2.27 \text{ W cm}^{-1} \text{ K}^{-1}$, assuming that there is no isotope scattering in GaN. This is very close to the measured values in high-quality freestanding GaN samples, the electrical properties of which are discussed in Volume 2, Chapter 3 and optical properties of which are discussed in Volume 2, Chapter 5.

Using a steady-state four-probe method and a high-quality freestanding GaN template, Slack *et al.* [91] measured a value for κ of $2.3 \text{ W cm}^{-1} \text{ K}^{-1}$ at room temperature, which increased to over $10 \text{ W cm}^{-1} \text{ K}^{-1}$ at 77 K. The method holds for four-probe thermal measurement, where the term “four probe” is analogous to the four-probe electrical measurement method. Namely, a heater is attached on the end of the sample – sandwiched in a copper clamp so that the heat flows through the entire width of the sample, not just the surface – supplying a heat current Q (analogous to an electrical current I). Two thermocouple junctions are attached along the length of the specimen by two little copper clamps separated by a distance L , the schematic representation of which is shown in Figure 1.21.

The heat current Q creates a temperature gradient of ΔT across the wafer. The κ value is calculated using $\kappa = (P/\Delta T)(L/A)$, where P is the power (=voltage \times current) supplied to the heater and A represents the cross-sectional area of the sample. Although the technique sounds simple, its accuracy depends very critically on making sure that the heat conduction is through the specimen and along the direction in which the temperature gradient is measured. To make certain that heat is transferred in the said direction only, the radiation losses must be minimized as well as making sure that the electrical wires used do not remove heat. To this end, the sample is placed in a turbo pumped vacuum to eliminate conduction and convection through the surrounding medium. Heat losses via conduction through the wires are minimized using long (10 cm), thin ($<100 \mu\text{m}$) wires of low thermal conductivity, typically chromel/constantan thermocouple and heater wires. Radiation losses are

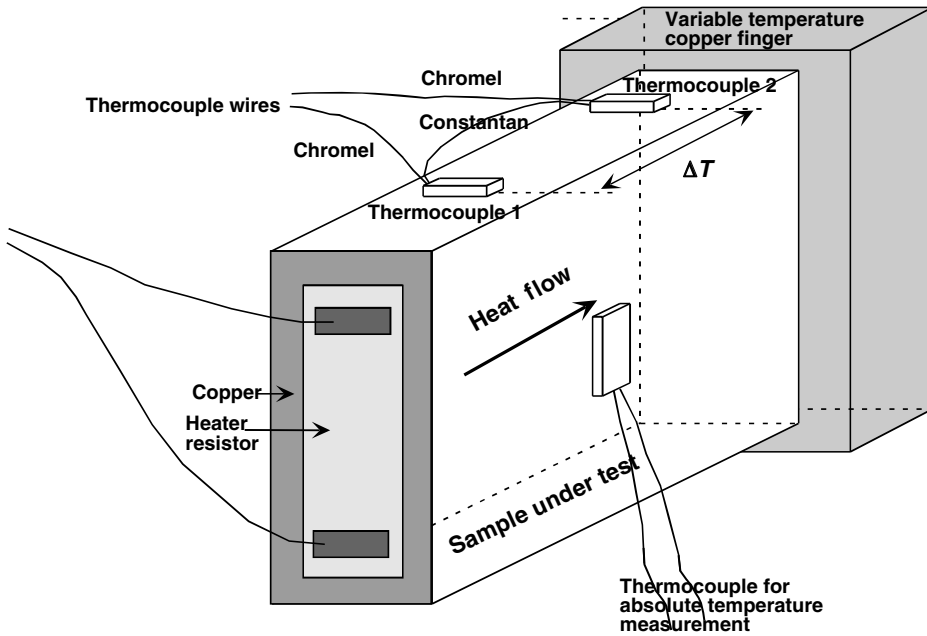


Figure 1.21 Schematic representation of the four-probe thermoelectric measurement setup used to measure the thermal conductivity of freestanding GaN [91].

minimized by surrounding the sample with a heat shield anchored thermally to the cold tip of the cryostat. By carefully designing this shield, Slack *et al.* [91] were able to reduce the total heat loss to the order of $1\text{--}2\text{ mW K}^{-1}$ at room temperature. Because the radiation losses follow T^3 dependence, they die off rather quickly below room temperature. For a sample with a thermal conductivity of $1\text{ W cm}^{-1}\text{ K}^{-1}$, cross section of $1 \times 3\text{ mm}^2$, and thermocouple probe separation of 5 mm , the thermal conductance is about 60 mW K^{-1} , so the heat losses are less than 5%. Fortunately, for wide bandgap semiconductors such as GaN the thermal conductivities are high enough so that the heat conduction is mainly through the sample, reducing the measurement error. Just as a reference point, for samples of lower thermal conductance (either lower conductivity or thinner), the heat losses can become important near room temperature. Thus, the samples for lower thermal conductivity materials (e.g., glasses or thermoelectric alloys) usually need to be short with large cross-sectional areas. The temperature-dependent thermal conductivity so measured for freestanding GaN is shown in Figure 1.22. From that temperature dependence and assuming the heat dissipation is through acoustic phonons, a *Debye temperature* of $\theta_D \approx 550\text{ K}$ was deduced, which compares with 650 K reported by Slack *et al.* [91].

As can be seen in Figure 1.22, the measured thermal conductivity of GaN in the temperature range of $80\text{--}300\text{ K}$ has a temperature power dependence of -1.22 . This slope is typical of pure adamantine crystals below the Debye temperature indicating acoustic phonon transport where the phonon–phonon scattering is a combination of

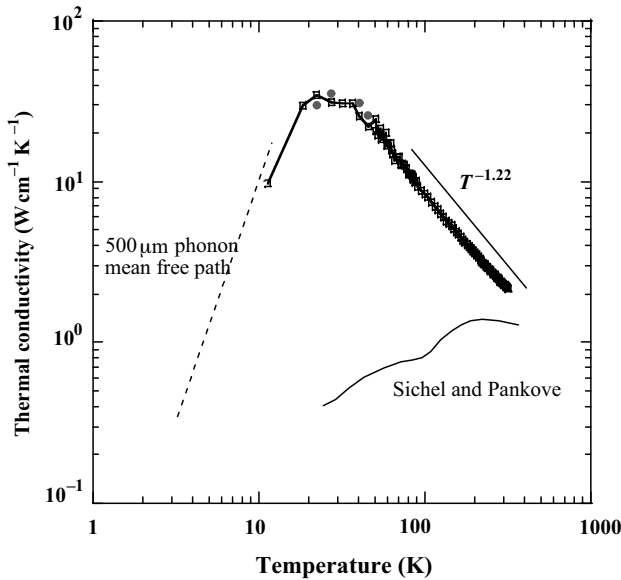


Figure 1.22 The thermal conductivity of 200 μm thick freestanding GaN sample (Samsung) as a function of temperature. The dashed line indicates calculation using the boundary scattering limit for a phonon mean free path of 500 μm . Also shown is the $T^{-1.22}$ dependence between about 80 and 300 K, and earlier results of Sichel and Pankove [207] measured using a 400 μm HVPE sample. Courtesy of Slack and Morelli [91].

acoustic–acoustic and acoustic–optic interactions. This temperature dependence strongly suggests that the thermal conductivity depends mainly on intrinsic phonon–phonon scattering and not on phonon–impurity scattering. Keep in mind that the net electron concentration in the measured film is about 10^{16} cm^{-3} and the hole concentration is in the 10^{15} cm^{-3} range. In addition, the dislocation density is low, about 10^6 cm^{-2} . It should be pointed out that the thermal conductivity degrades with increased dislocation density, particularly above 10^7 cm^{-2} , with a slope of $0.4 \text{ W cm}^{-1} \text{ K}^{-1}$ per decade dropping down to slightly above $1 \text{ W cm}^{-1} \text{ K}^{-1}$ for a dislocation density of mid- 10^9 cm^{-2} . The dashed curve at low temperatures in Figure 1.22 has been calculated for boundary scattering assuming a mean free path of 500 μm [91]. The mean free path is comparable with the average sample diameter, which indicates that impurity scattering in this region is not dominant either.

The thermal conductivity of GaN is a tensor quantity and has two principal values κ_{\perp} and κ_{\parallel} perpendicular and parallel to the c -axis, respectively, that is, in-plane and out-of-plane values. The anisotropy in the sound velocity, which relates to the phonon propagation velocity, has been calculated by Polian *et al.* [38] in the form of $v_{\perp} = 5.56 \times 10^5 \text{ cm s}^{-1}$ and $v_{\parallel} = 5.51 \times 10^5 \text{ cm s}^{-1}$ for in-plane and out-of-plane directions, respectively. These values are smaller than the measured values, reported by Deger *et al.* [165], of $v_{\perp} = 8.02 \times 10^5 \text{ cm s}^{-1}$ and $v_{\parallel} = 7.79 \times 10^5 \text{ cm s}^{-1}$ for in-plane

and out-of-plane directions, respectively. The in-plane and out-of-plane sound velocities reported in Ref [36] are tabulated in Tables 1.7 and 1.9 for wurtzitic and zinc blende phases of GaN. Because the difference is negligible and the anharmonicity producing the phonon–phonon scattering is not discernible, one can conclude that in-plane thermal conductivity measurements are a good representative of κ in GaN [91].

A newer method, named the scanning thermal microscopy (SThM) [209], has been developed to measure thermal conductivity and is purported to provide nondestructive, absolute measurements with a high spatial/depth resolution of about 2–3 μm . Thermal imaging is achieved using a resistive thermal element incorporated at the end of a cantilever/AFM-type feedback as shown in Figure 1.23. The resistive tip forms one element of a Wheatstone bridge as shown in Figure 1.24. The spatial/depth resolution is estimated to be $\sim 2\text{--}3\ \mu\text{m}$ for GaN and AlN. Upon contact with the sample, the tip tends to cooldown due to heat conduction into the sample, which is related to its thermal conductivity, κ . The bridge circuit applies a compensating voltage (U_{out}) to maintain its target operating temperature. The feedback signal for constant resistance is a measure of the thermal conductivity of the material with which the tip is in contact, specifically V_{out}^2 is proportional to κ because power dissipation is the mechanism here. Measurements of the absolute values of κ are based on a calibration procedure. This simply comprises calibrating the feedback signal, V_{out}^2 , for a constant thermal element resistance against that for samples with known conductivities such as GaSb, GaAs, InP, Si, and Al metal, as shown in Figure 1.25. The influence of the surface roughness on the effective thermal conductivity is of concern. For a perfectly flat surface,

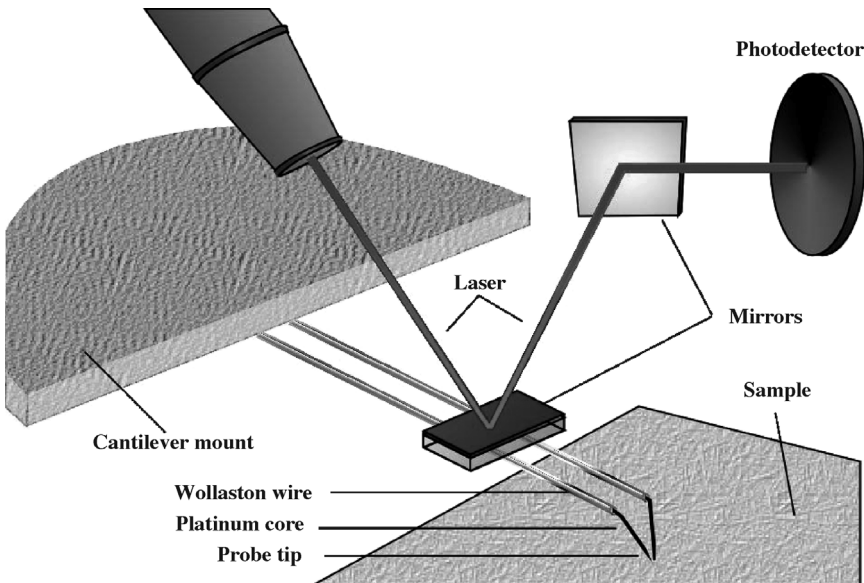


Figure 1.23 An artist's view of the scanning thermal microscope. Patterned after D.I. Florescu and F.H. Pollak. (Please find a color version of this figure on the color tables.)

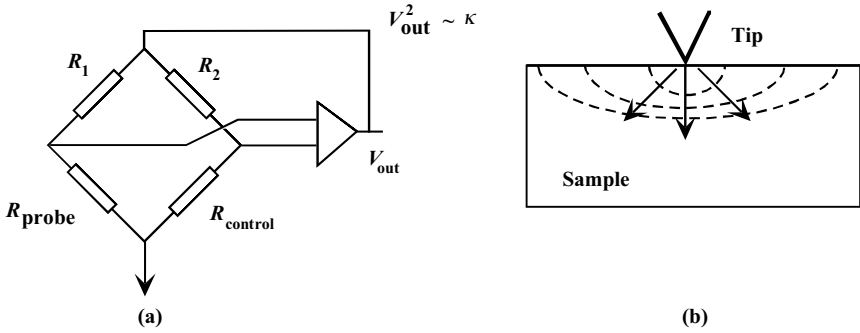


Figure 1.24 (a) Wheatstone bridge arrangement in which the tip temperature is kept constant before and after contact with the material whose thermal conductivity is being measured. The feedback signal U_{out} is related to thermal conductivity, κ . A calibration against known samples such as Si, GaAs, GaP, and so on, leads to absolute values of κ . (b) Schematic diagram of heat dissipation into the sample from the tip. Courtesy of D.I. Florescu and F.H. Pollak.

the contact between the probe tip (radius of curvature ~ 1 fm) and the sample surface is very small. For rough surfaces, however, the tip could impinge on a valley- or hillocklike feature with the valley/hillock leading to increased/decreased thermal signal accompanied by a corresponding change in the measured effective thermal conductivity.

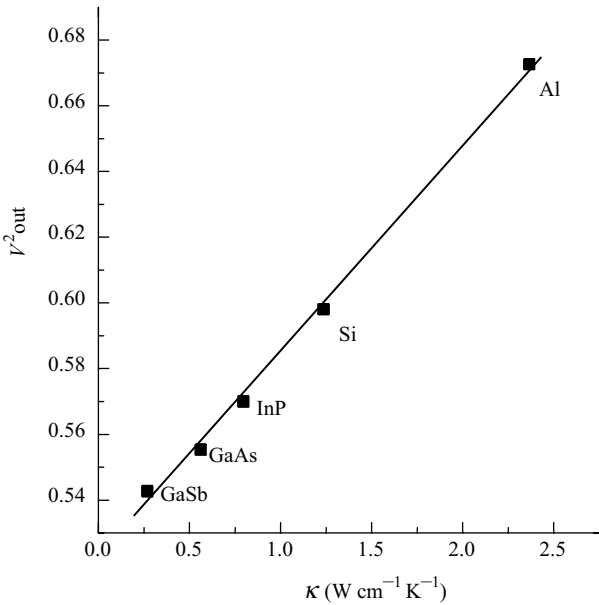


Figure 1.25 The feedback signal, V_{out}^2 , which is a measure of the thermal conductivity of the material under test, for a constant thermal element resistance for samples with known conductivities such as GaSb, GaAs, InP, Si, and Al metal. Courtesy of D.I. Florescu and F.H. Pollak.

The SThM method has been applied to the measurement of the room-temperature thermal conductivity on both fully and partially coalesced epitaxial lateral overgrown GaN/sapphire (0001) samples [209]. As expected, a correlation between low threading dislocation density and high thermal conductivity values was established. The reduction in the thermal conductivity with increased dislocation density is expected as threading dislocations degrade the sound velocity and increase the phonon scattering in the material. In fact, due to the high defect concentrations in early films, the thermal conductivity value measured was $1.3 \text{ W cm}^{-1} \text{ K}^{-1}$ [207]. Using this method, the highest GaN κ values, $2.0\text{--}2.1 \text{ W cm}^{-1} \text{ K}^{-1}$, were found in the regions of the samples that were laterally grown and thus contained the lowest density of threading dislocations. This compares with a value of $2.3 \text{ W cm}^{-1} \text{ K}^{-1}$ in a freestanding sample measured by the steady-state four-probe method discussed earlier. Even then, it falls short of the predictions by Witek [208].

An explanation for the dramatic increase from to $\kappa \sim 1.3 \text{ W cm}^{-1} \text{ K}^{-1}$ for the early samples to $2.3 \text{ W cm}^{-1} \text{ K}^{-1}$ for the freestanding sample, as iterated above is most likely related to extended defect concentration (D_d) and the differences in background doping. The effect of dislocation density on the thermal conductivity has been calculated by Kotchetkov *et al.* [210]. The dislocation density in the thick film measured by Sichel and Pankove was between 10^9 and 10^{10} cm^{-2} , while the freestanding sample exhibited densities of less than 10^6 cm^{-2} near the top surface (Ga-polarity) and 10^7 cm^{-2} near the bottom surface (N-polarity). Kotchetkov *et al.* showed that κ remains fairly independent of D_d up to some characteristic value D_d^{char} after which it decreases about a factor of 2 for every decade of increase in D_d .

The thermal conductivity has also been correlated to doping levels in HVPE n-GaN/sapphire (0001) by SThM on two sets of samples [211,212]. In both sets of data, the thermal conductivity decreased linearly with $\log n$, n being the electron concentration, the variation being about a factor of 2 decrease in κ for every decade increase in n . Significantly, it was concluded that the decrease in the lattice contribution to κ , due to increased phonon scattering from impurities and free electrons, predominates the increase in the electronic contribution. Also, a correlation between the film thickness and the improved thermal conductivity was found, which is consistent with the observed general reduction of both extended (dislocations) and point defects with film thickness [212].

The κ values at 300 K before and after plasma-induced effects on a series of n-GaN/sapphire (0001) samples fabricated by HVPE were also measured [213]. The sample thicknesses were $50 \pm 5 \mu\text{m}$ and the carrier concentrations were $\sim 8 \times 10^{16} \text{ cm}^{-3}$, as determined by Hall effect measurements. The thermal conductivity before treatment was found to be in the $1.70\text{--}1.75 \text{ W cm}^{-1} \text{ K}^{-1}$ range, similar to that previously reported for HVPE material with this carrier concentration and thickness [211,212]. The κ value was reduced, however, when the samples were processed under constant Ar gas flow and pressure for a fixed period of time (5 min). The only variable processing parameter was the DC bias voltage (125–500 V). After the initial 125 V procedure, κ exhibited a linear decrease with the DC voltage in the investigated range. At 125 V, the thermal conductivity was only slightly less ($\kappa \sim 1.65 \text{ W cm}^{-1} \text{ K}^{-1}$)

than the untreated case. The values of κ had dropped to $\sim 0.3 \text{ W cm}^{-1} \text{ K}^{-1}$ for the 500 V case.

To a first extent, the temperature dependence of the specific heat of Wz GaN (C_p) at constant pressure can be expressed by phenomenological expression [51]. In this vein, the specific heat C_p of Wz GaN at constant pressure for $298 \text{ K} < T < 1773 \text{ K}$ can be expressed as

$$\begin{aligned} C_p(T) &= 9.1 + (2.14 \times 10^{-3} T) (\text{J mol}^{-1} \text{ K}^{-1}), \\ C_p &= 38.1 + 8.96 \times 10^{-3} T (\text{cal mol}^{-1} \text{ K}^{-1}) \quad (1 \text{ cal} = 4.186 \text{ J}). \end{aligned} \quad (1.15)$$

However, this expression is very simplistic, as will be seen below. As already mentioned, free electrons (very effective at low temperatures), impurities, defects (inclusive of point defects), and lattice vibrations contribute to specific heat. If GaN with negligible free-electron concentration and defects were available, only the lattice contribution would be considered, which is also the case in texts [214]. The specific heat of Wz GaN has been studied by Koshchenko *et al.* [215] in the temperature range of 5–60 K and also by Demidienko *et al.* [216] in the temperature range of 55–300 K and discussed by Krukowski *et al.* [88,127]. The Debye expression for the temperature dependence of specific heat in a solid at a constant pressure (C_p) can be expressed as [214]

$$C_p = 18R \left(\frac{T}{\theta_D} \right)^3 \cdot \int_0^{x_D} \frac{x^4 e^x}{(e^x - 1)^2} dx, \quad (1.16)$$

where $x_D \equiv \theta_D/T$ and $R = 8.3144 \text{ J mol}^{-1} \text{ K}^{-1}$ is the molar gas constant. The coefficient in front of the term R has been multiplied by 2 to take into account the two constituents making up the binary GaN. By fitting the measured temperature-dependent heat capacity to the Debye expression, one can obtain the *Debye temperature* θ_D specific to heat capacity. The experimental data of Demidienko *et al.* and Krukowski *et al.* are plotted in Figure 1.26. Also shown in the figure is the calculated specific heat using the Debye expression for Debye temperatures of 500, 600, 700, and 800 K. It is clear that the quality of the data and/or sample prevents attainment of a good fit between the experimental data and Equation 1.16. Consequently, a Debye temperature with sufficient accuracy cannot be determined. It is easier to extract a Debye temperature using data either near very low temperatures or well below the Debye temperature where the specific heat has a simple cubic dependence of temperature [214]:

$$C_p = 234R \left(\frac{T}{\theta_D} \right)^3. \quad (1.17)$$

Unfortunately, the GaN samples contain large densities of free carriers and defects that compromise the application of the Debye specific heat expression. Consequently, a good fit to the data is not obtained and the Debye temperature so extracted is not as dependable as desired.

There is a spread in the reported Debye temperatures for GaN, θ_D , in the range of about 600 to 700 K. Slack [77] estimated a value of 600 K at 0 K by utilizing the more established Debye temperatures for BeO and AlN. This compares with 550 K deduced

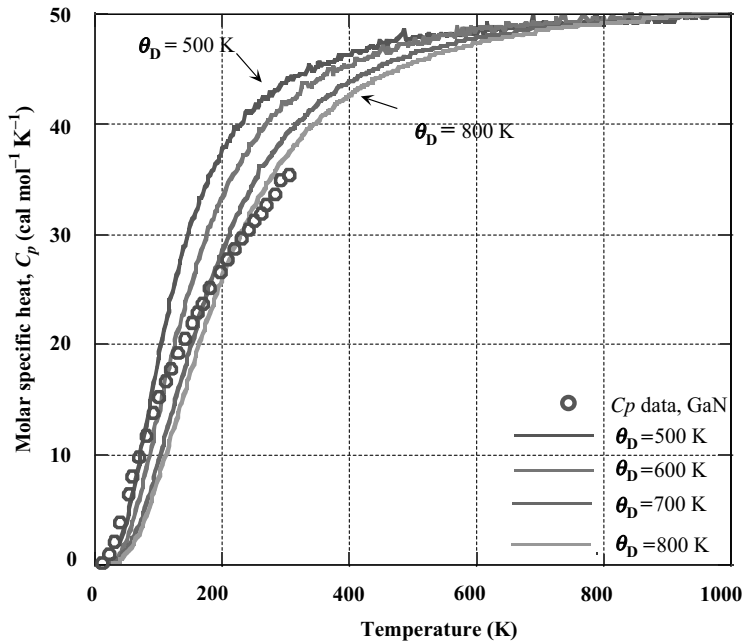


Figure 1.26 Molar specific heat at constant pressure, C_p ($\text{cal mol}^{-1} \text{K}^{-1}$), of GaN versus temperature. Open circles represent the experimental data. The solid lines are calculation based on the Debye model for Debye temperatures, θ_D , of 500, 600, 700, and 800 K. Unfortunately, it is difficult to discern a Debye temperature that is effective over a wide

temperature range because a large concentration of defects and impurities is present in GaN. However, a value of 600 K estimated by Slack is used commonly. The data are taken from Refs [215,216], as compiled in Ref. [88]. (Please find a color version of this figure on the color tables.)

from heat transfer due to acoustic phonons, as mentioned above. Because the samples used in these measurements contained defects and large density of free electrons, the dispersion among the data and Debye expression is attributed to defects at high temperatures and free electrons at low temperatures. Elastic properties of GaN can also be used to deduce the Debye temperature. In this vein, Raman scattering measurements yielded a Debye temperature of $\theta_D = 650 \text{ K}$ [38]. Calculations since the estimate of Slack [77] yielded a range of 620–690 K [88].

Thermodynamic properties of Wz GaN have been reported by Elwell and Elwell [217]. From the reaction



the *heat of formation* of Wz GaN was calculated to be $\Delta H_{298 \text{ K}} = -26.4 \text{ kcal mol}^{-1}$ [217], or as the standard heat of formation $\Delta H = -37.7 \text{ kcal mol}^{-1}$ [194]. The equilibrium vapor pressure of N_2 over solid GaN has been found to be 10 MPa at 1368 K and 1 GPa at 1803 K [202]. A thorough description of the GaN phase diagram including the equilibrium vapor pressure of N_2 over GaN as well as AlN and InN has been presented by Porowski and Grzegory [218] (1 cal = 4.186 J).